Helsinki University of Technology Laboratory of Biomedical Engineering
Department of Engineering Physics and Mathematics

Teknillinen korkeakoulu Lääketieteellisen tekniikan laboratorio
Teknillisen fysiikan ja matematiikan osasto
Espoo 2004

INSTRUMENTATION FOR MEDICAL OPTICAL TOMOGRAPHY WITH APPLICATIONS

Ilkka Nissilä

TEKNILLINEN KORKEAKOULU
TEKNISKA HÖGSKOLAN
HELSINKI UNIVERSITY OF TECHNOLOGY
TECHNISCHE UNIVERSITÄT HELSINKI
UNIVERSITE DE TECHNOLOGIE D'HELSINKI

Helsinki University of Technology Laboratory of Biomedical Engineering
Department of Engineering Physics and Mathematics

Teknillinen korkeakoulu Lääketieteellisen tekniikan laboratorio
Teknillisen fysiikan ja matematiikan osasto
Espoo 2004

INSTRUMENTATION FOR MEDICAL OPTICAL TOMOGRAPHY WITH APPLICATIONS

Ilkka Nissilä

Dissertation for the degree of Doctor of Science in Technology to be presented with due permission of the Department of Engineering Physics and Mathematics, Helsinki University of Technology for public examination and debate in lecture room F1 of the physics building at Helsinki University of Technology (Espoo, Finland) on the 10th of December, 2004, at 12 o'clock noon.

Helsinki University of Technology
Department of Engineering Physics and Mathematics
Laboratory of Biomedical Engineering

Teknillinen korkeakoulu
Teknillisen fysiikan ja matematiikan osasto
Lääketieteellisen tekniikan laboratorio

ISBN 951-22-7413-2 (printed version)
ISBN 951-22-7414-0 (electronic version)
Picaset Oy, Helsinki 2004

HELSINKI UNIVERSITY OF TECHNOLOGY
P.O. BOX 1000, FIN-02015 HUT
http://www.hut.fi

ABSTRACT OF DOCTORAL DISSERTATION

Author Ilkka Tapani Nissilä

Name of the dissertation

Instrumentation for medical optical tomography with applications

Date of manuscript November 4, 2004 | Date of the dissertation December 10, 2004

☐ Monograph ☑ Article dissertation (summary + original articles)

Department Department of Engineering Physics and Mathematics
Laboratory Laboratory of Biomedical Engineering
Field of research Medical imaging, biomedical optics
Opponent Dr. Maria Angela Franceschini
Supervisor Prof. Toivo Katila

Abstract

Near-infrared spectroscopy (NIRS) and imaging techniques based on it are a field which has been the subject of intensive research during the past 15 years. In NIRS, the tissue is illuminated with visible red or near-infrared (NIR) light of several wavelengths, and the light which is reflected back from the tissue or transmitted through it is measured using sensitive photodetectors. As the distance between the source and the detector is increased, the sensitivity of the measured intensity of light to changes in the internal parts of the tissue increases. Two main optical parameters can be defined which characterize the tissue: the scattering and absorption coefficients. The absorption coefficient is sensitive to the concentrations of oxygenated and deoxygenated hemoglobins in the tissue. The partial blood volume and oxygen saturation in the tissue studied can be calculated if the concentrations are known. The optical measurements are non-invasive and patient-friendly, and they can be performed in the presence of electromagnetic interference. The most interesting applications of optical imaging include the imaging of hemodynamic changes related to neural activity in adults and infants, the imaging of hematoma and circulatory defects in premature infants, mammography, and imaging of muscle tissue during exercise. The goal of this thesis was to develop a multichannel intensity-modulated optical imaging system, which can be used for the imaging of activation-related hemodynamic changes in the adult and neonatal cortex as well as optical tomography. The system can be calibrated to give absolute measurements of amplitude and phase, which reflect the absolute attenuation and temporal delay of the light as it passes through the tissue from source to detector. Both difference imaging (imaging of the differences between two functional states of a tissue, or between two phantoms) and absolute imaging are successfully demonstrated using phantoms which have realistic background values close to the optical properties of premature neonates' heads, and small targets with contrasts that occur between background tissue and, e.g., breast cancer, bone, or hematoma. Many activation measurements were also performed successfully using the system, including the measurement of hemodynamic changes in the right motor cortex during transcranial magnetic stimulation of the left motor cortex in adults, as well as bilateral auditory activation measurements on healthy full-term neonates.

Keywords Optical tomography, intensity modulation, instrumentation, near-infrared spectroscopy, activation studies

UDC | Number of pages 198

ISBN (printed) 951-22-7413-2 | ISBN (pdf) 951-22-7414-0

Publisher Helsinki University of Technology, Laboratory of Biomedical Engineering

Print distribution

☑ The dissertation can be read at http://lib.hut.fi/Diss/ 2004/isbn9512274140

Preface

This work has been carried out in the Laboratory of Biomedical Engineering, Helsinki University of Technology and the BioMag Laboratory of Helsinki University Central Hospital. The financial support by the graduate school Functional Research in Medicine, the Jenny and Antti Wihuri Foundation, the National Technology Agency of Finland (TEKES), the Instrumentarium Science Foundation, the Foundation of Technology (TES), the Academy of Finland, and the Cognitive Brain Research Unit, Department of Psychology, University of Helsinki is greatly acknowledged. I also appreciate the support of GE Medical Systems Finland (formerly Instrumentarium Oyj, Datex-Ohmeda group), Nexstim Oy, and DBC Finland.

I would like to thank Professor Toivo Katila for his support of my work and our project. I would also like to thank Dr. Minna Huotilainen, Professor Vineta Fellman and Professor Risto Näätänen for initiating the project on optical measurements on infants and their support. Professor Pekka Meriläinen was very helpful in creating ties with the industry, which was essential.

I am grateful to Professor Jari Kaipio and Professor Arjun Yodh for their careful review of my thesis and the improvements they suggested. I would also like to thank Dr. Timo Kajava for reading my thesis very carefully.

I am much in debt to the members of our research group. Thank you for creating a pleasant and enthusiastic atmosphere at work. In particular, M. Sc. Kalle Kotilahti has been a good friend and he has shared many of the less fun but necessary parts of the work with me. I am grateful to M. Sc. Tommi Noponen and Lauri Lipiäinen for their part in the design and construction of the instrument. They have always been keen to improve things beyond perfection.

I would like to thank M. Sc. Jenni Heino for our many discussions on optical tomography and her advice. In addition, I would like to thank M. Sc. Petri Lipponen, M. Sc. Petra Sohlman, and Petri Hiltunen for their contributions. I am grateful to M. Psych. Merja Hotakainen, Nasia Gavrielides and Riikka Mäkelä for their help with the neonatal project and especially RN Tarja Ilkka for her important contribution.

I am grateful to M. Sc. Tanja Tarvainen and Professor Jari Kaipio for developing and sharing the interchannel offset calibration algorithm.

M. Sc. Kim Fallström deserves my greatest respect for his impeccable insight and analysis of my problems in radiofrequency electronics. Thank you also to Dr. Mikko Merimaa, Dr. Tapio Niemi and Professor Matti Kaivola for their expertise in optics and electronics.

To M. Sc. Soile Komssi, Dr. Seppo Kähkönen, and Dr. Risto Ilmoniemi I am indebted for their help in the TMS experiments.

I would like to thank Professor Jeremy Hebden for lending me his excellent phantoms and for his collaboration. Professor Simon Arridge has been supportive of my work and I much appreciate it. I owe Simon and Dr. Martin Schweiger a lot for their help with the reconstructions.

I can't really thank my father enough for his practical advice and mechanical engineering support, which have been enlightening and educative. I would like to thank my parents for their patience and support. Finally, Leena has shared many of my worries for too little in return - thank you for everything.

Otaniemi, November 15, 2004

Ilkka Nissilä

Contents

List of publications

This thesis consists of an overview and the following six publications:

I I. Nissilä, T. Noponen, J. Heino, T. Kajava, and T. Katila, Diffuse optical imaging, *Advances in Electromagnetic Fields in Living Tissue* **4**, Ed. J. C. Lin, Springer Science (2005, in press).

II I. Nissilä, K. Kotilahti, K. Fallström, and T. Katila, Instrumentation for the accurate measurement of phase and amplitude in optical tomography, Rev. Sci. Instrum. **73**: 3306-12 (2002).

III I. Nissilä, T. Noponen, K. Kotilahti, T. Tarvainen, M. Schweiger, L. Lipiäinen, S. Arridge, and T. Katila. Instrumentation and calibration methods for the multichannel measurement of phase and amplitude in optical tomography, Helsinki University of Technology Report TKK-F-A833 (2004).

IV I. Nissilä, J. C. Hebden, D. Jennions, J. Heino, M. Schweiger, K. Kotilahti, T. Noponen, A. Gibson, S. Järvenpää, L. Lipiäinen, and T. Katila. A comparison between difference data measured with a time-domain and a frequency-domain system for optical tomography, Helsinki University of Technology Report TKK-F-A834 (2004).

V I. Nissilä, K. Kotilahti, S. Komssi, S. Kähkönen, T. Noponen, R. J. Ilmoniemi, and T. Katila. Optical measurement of hemodynamic changes in the contralateral motor cortex induced by transcranial magnetic stimulation. Proceedings of the 13th International Conference on Biomagnetism, Jena, Germany, pp. 851-4 (2002).

VI I. Nissilä, K. Kotilahti, M. Huotilainen, R. Mäkelä, L. Lipiäinen, T. Noponen, N. Gavrielides, R. Näätänen, V. Fellman, and T. Katila. Auditory hemodynamic studies of newborn infants using near-infared spectroscopic imaging. Proceedings of the 26th Annual International Conference of the IEEE Engineering in Medicine and Biology Society, San Francisco, California, USA, pp. 1244-7 (2004).

Abbreviations

Abbreviation	*Explanation*
AC	Alternating current
APD	Avalanche photodiode
BOLD	Blood oxygenation level dependent contrast
BW	Bandwidth
CBF	Cerebral blood flow
CNR	Contrast-to-noise ratio
CSF	Cerebrospinal fluid
CT	Computed Tomography (3D imaging with X rays)
DA	Diffusion approximation (to the RTE)
DC	Direct current
DE	Diffusion equation
DPF	Diffuse pathlength factor
EEG	Electroencephalography
ENI	Equivalent-noise intensity, the same as NEP
FE	Finite element
FEM	Finite element method
IF	Intermediate frequency
IIR	Infinite impulse response
LD	Laser diode (semiconductor laser)
LIA	Lock-in amplifier
MBLL	Modified Beer-Lambert Law
MEG	Magnetoencephalography
MONSTIR	The time-domain optical tomography system developed at UCL
MR	Magnetic resonance
MRI	Magnetic Resonance Imaging
NA	Numerical aperture
ND	Neutral density
NEP	Noise-equivalent power
NF	Noise figure
NIRS	Near-infrared spectroscopy
NIRSI	Near-infrared spectroscopic imaging

Abbreviation	*Explanation*
NTC	Negative Temperature Coefficient
PET	Positron Emission Tomography
PMT	Photomultiplier tube
QE	Quantum efficiency
RF	Radiofrequency
RTE	Radiative transfer equation, also called the Boltzmann transport equation
RTSI	Real-time system integration
SiPD	Silicon photodiode
SNR	Signal-to-noise ratio
SPECT	Single-Photon Emission Computed Tomography
TMS	Transcranial magnetic stimulation
TPSF	Temporal point-spread function
UCL	University College London
VOA	Variable optical attenuator

List of symbols

Symbol	*Explanation*
μ_a	Absorption coefficient
μ_s	Scattering coefficient
μ_s'	Reduced scattering coefficient
g	Anisotropy factor, mean cosine of scattering angle
n	Index of refraction
c	Speed of light
$\mu_\mathrm{a,bg}$	Absorption coefficient of the background
$\mu_\mathrm{s,bg}'$	Reduced scattering coefficient of the background
$\mathbf{r}$	Position
$\hat{\mathbf{s}}$	Direction of propagation of light
Θ	Scattering phase function
L	Radiance
q	Source term
κ	Diffusion coefficient
Φ	Photon density
η	Quantum efficiency, QE
Δf	Bandwidth of the measurement
I_d	Dark current
I_photon	Photon shot noise current
e	Charge of electron
M	Gain of an APD
χ	Excess noise index
δ	Secondary emission ratio of a dynode, typically ≈ 6 at maximum gain
μ	Gain of a PMT
i_q	Quiescent current

1 Introduction

1.1 Background

Medical imaging is a field which has experienced rapid development during the past 25 years. Techniques such as x-ray computed tomography (CT)[1] and magnetic resonance imaging (MRI)[2] allow precise anatomical characterisation of tissues with a spatial resolution of the order of 1 mm. Different tissue types, structural damage, infections, and cancer can be detected using these techniques. The imaging times of these techniques have gradually been reduced, and today it is possible to use them for functional imaging. For example, x-ray CT can be used to study the function of the heart[3], and MRI can be used to study hemodynamic changes in the brain[4].

Functional imaging techniques allow the imaging of tissue physiology, e.g., blood flow, tissue metabolism, and digestive processes. These techniques include positron emission tomography (PET)[5] and single photon emission computed tomography (SPECT)[5], which both require the use of radioisotopes injected into the blood. Most functional imaging techniques have considerably lower spatial resolution than the anatomical imaging modalities, but they provide information which would otherwise require more invasive procedures such as biopsy.

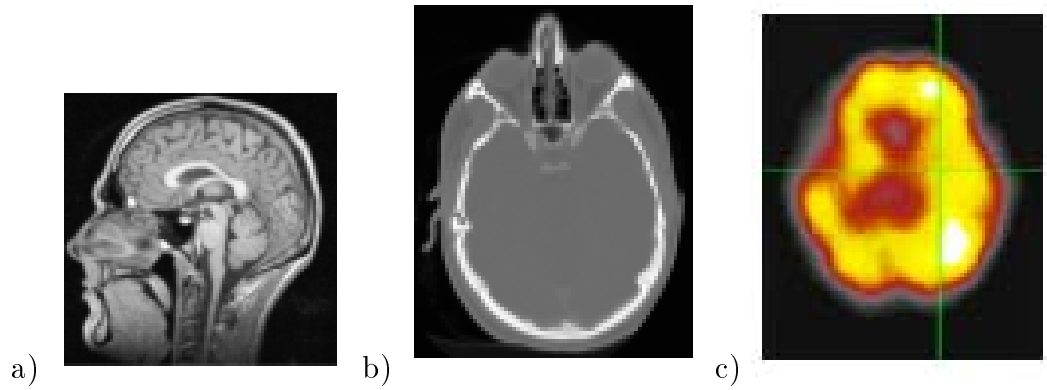

Figure 1. Two-dimensional slices of a) an anatomical MR image, b) an anatomical CT image, and c) a functional (PET) image of the brain.

Near-infrared spectroscopy (NIRS) was first shown to be able to detect changes in the concentrations of oxygenated and deoxygenated hemoglobin (HbO_2 and Hb) in the living brain non-invasively by Jöbsis in 1977[6]. It is usually implemented using a single source fiber with several wavelengths, and one or a few detectors. Due to the strong scattering in tissue, the contrast due to absorption changes inside the tissue is low, and the spatial resolution is modest. However, the technique is completely non-invasive and it can be applied to study the female breast[7], muscles[8], and cerebral hemodynamics[9]. Optical

imaging can be implemented so that the instrument is transportable, it can be used for bedside applications, and it is insensitive to external electromagnetic disturbances except for light itself. Several groups are studying optical imaging with the goal of developing it into a clinically useful tool[10–27]. The most attractive applications for optical imaging are optical mammography and functional brain imaging. At present, optical imaging looks promising and the potential of the method has been demonstrated in several applications, but sensitivity, reliability, and ease of use need to be improved further for it to become a clinical tool.

1.2 Goals of the thesis

Two main goals were set for this thesis. First, a multichannel optical tomography system based on the use of radiofrequency intensity modulated light was to be designed and implemented together with the research group. The author's role was to be the main architect of the system and to either implement or instruct the implementation of the components of the system as used in this work. The frequency-domain (FD) principle was chosen instead of time-domain (TD) or continuous-wave (CW, also known as direct current (DC)) as it was considered to provide a good compromise between information content and cost. Methods for the calibration and use of the measured data for optical tomography were to be developed. A second major goal for the instrument was that it should be possible to image the hemodynamic response related to cortical activation using the system.

The overview is structured in the following way: In section 2, optical tomography is introduced along with a discussion on the separation of the scattering and absorption within the tissue. A set of reconstructions based on simulated data with added gaussian noise are given to illustrate the requirements on the quality of data. In section 3, the basics of optical activation imaging are discussed including some aspects of instrumental requirements and the possibility of modeling the optical structure of the head. In section 4, the most important aspects in the design of the frequency-domain instrument are described. An example of a reconstruction from measured data is given in section 5. In section 6, two activation experiments are described along with experiences obtained from them. Concluding remarks are given in section 7.

2 Optical tomography

Optical tomography is a method for the imaging of the internal optical properties of tissue using near-infrared (NIR) or visible red light. The optical properties of different tissue types differ significantly. The sensitivity of a particular measurement to changes in the optical properties at a particular location inside the tissue depends on the optical properties of the background tissue. The knowledge of the distribution of optical properties of the tissue should improve the quantitative accuracy of the measured changes in [HbO_2] and [Hb] as well as allowing the estimation of the baseline concentrations of HbO_2 and Hb[28].

In optical tomography, measurements are made using a set of light sources and detectors (or optical fibers) placed on the surface of the tissue. Using the data obtained from these measurements, images of the scattering and absorption coefficients (μ'_s and μ_a) inside the tissue are generated using an image reconstruction algorithm. The reconstruction methods are usually iterative. From an initial starting guess of the optical properties, a simulated data set is calculated and compared with the measured data. The optical property distribution in the model is updated to minimize the difference between the simulated and measured data. This process is continued until the algorithm converges or an otherwise satisfactory result is obtained.[29]

In the case of complex optical structures, such as those found in the human head, it would be advantageous to use external *a priori* information from MRI or x-ray CT to define the boundaries between the different tissue types precisely. This information can be used in various ways to improve the reconstructions of the optical properties or changes in them.[30–33] For example, regional constraints in the optical properties can be defined.

2.1 Instrument types

Three basic instrument types are used in optical tomography. The DC instruments measure ms–range pulses of light and they provide a measure of the attenuation of light in the tissue between the source and the detector[34–39]. Frequency-domain systems use radiofrequency (RF) modulated light and measure the phase shift and amplitude attenuation of the photon density wave[40–45]. Most CW and FD systems provide measurements of changes in the intensity, amplitude, and phase shift, instead of absolute values. Time-domain systems use picosecond-range pulses of light and measure the temporal point spread function (TPSF), which is the distribution of photon propagation times in the tissue. Calibration techniques for time-domain data types are discussed by Hillman et al.[46] and Hebden et al.[47]. A technique for interchannel offset calibration for DC data has been published by Schmitz et al.[34] and for the amplitude and phase by Tarvainen et al.[48]

2.2 Limitations

Optical tomography can only be applied to relatively thin tissue samples of at most about 9-11 cm in diameter, depending on the system and the optical properties of the particular tissue studied. This is due to the exponential attenuation of light in tissue, the quantum nature of light, and limitations in the optical power which can be safely used to study living tissue.

Images of tissues with a low contrast between the tissue types produce images of lower quality than those which have high-contrast features. The intrinsic ability of optical tomography to resolve features in scattering is better than in absorption; the scattering features are reconstructed with better contrast recovery and higher spatial resolution.

Ideally, optical tomography should give the user consistent and predictable images of scattering and absorption in tissue with a good quantitative accuracy. If *a priori* information is needed to resolve non-uniqueness issues and reduce the effects of noise on the images, it should be based on information which the user or instrument designer can provide from their knowledge of the systematic and stochastic errors present in the measurements.

2.3 Modeling of light propagation

A widely used model for describing light propagation in random media is the radiative transfer equation (RTE)[29]

$$\left(\frac{1}{c}\frac{\partial}{\partial t} + \hat{\mathbf{s}}\cdot\nabla + \mu_s(\mathbf{r}) + \mu_a(\mathbf{r})\right) L(\mathbf{r},\hat{\mathbf{s}},t) = \mu_s(\mathbf{r})\int \Theta(\hat{\mathbf{s}}\cdot\hat{\mathbf{s}}')L(\mathbf{r},\hat{\mathbf{s}},t)\,\mathrm{d}\hat{\mathbf{s}}' + q(\mathbf{r},\hat{\mathbf{s}},t), \quad (1)$$

where c is the speed of light in the medium, $\mathbf{r}$ and t are the position and time, $\hat{\mathbf{s}}$ is the direction of propagation, Θ is the scattering phase function, L is the radiance (in $\mathrm{Wm^{-2}sr^{-1}}$), and q is the light source. The RTE describes how the energy radiance L changes in time due to photon transfer through the medium, subject to scattering and absorption processes.

The equation treats light as photons, ignoring interference effects, because the photons travel through the tissue in random paths and the coherence of light is lost within a few millimeters from the light source which has been placed on the surface of the tissue.

Equation 1 is computationally difficult and it is not yet practical to use it as the light-propagation model in optical tomography. If $\mu_\mathrm{s}' >> \mu_\mathrm{a}$ and the observation point is far from the light source, a simpler model may be derived by integrating over the light propagation angles to obtain

$$-\nabla\cdot\kappa(\mathbf{r})\nabla\Phi(\mathbf{r},t) + \mu_a\Phi(\mathbf{r},t) + \frac{1}{c}\frac{\partial\Phi(\mathbf{r},t)}{\partial t} = q_0(\mathbf{r},t), \quad (2)$$

in which $\kappa = \frac{1}{3(\mu_a+\mu_s(1-g))}$, $g = E\{cos(\hat{\mathbf{s}}\cdot\hat{\mathbf{s}}')\}$, and $\Phi(\mathbf{r},t) = \int L(\mathbf{r},\hat{\mathbf{s}},t)\,\mathrm{d}\hat{s}$.

This equation is known as the diffusion equation (DE) and it is computationally reasonable even in 3D. A variety of inverse problem solution methods have been devised around it[29]. However, the approximation does not give correct results if low-scattering regions such as the cerebrospinal fluid (CSF) are present in the tissue[49]. In addition, the DE and RTE give different solutions close to the light source. In practice, the source-detector pairs which have a short separation (< 30 mm) are left out of the data to avoid this problem.

2.4 Reconstruction methods

Linear and non-linear reconstruction techniques have been devised using the diffusion equation as the light propagation model[50–61]. In either case, an initial guess of optical properties is needed. This can be obtained, e.g., by fitting the optical properties of a homogeneous model to the measured data. The Jacobian of the mapping between the material parameters and the measurements is calculated, and used to adjust the material properties in the model to minimize the difference between simulated and measured data. In a linear algorithm, this is done in a single step, while in a non-linear algorithm, the process of calculating the Jacobian, updating the model, and calculating the simulated data is repeated iteratively until the reconstruction converges or the result is otherwise considered to be satisfactory. In general, linear methods are used when computational speed has a priority and a qualitative result is sufficient. Non-linear algorithms give better quantitative accuracy but the practical reconstruction times are usually measured in hours for a 3D problem, while a linear algorithm might give the images in minutes or even seconds.

To calculate the reconstructions for this thesis, a regularized Gauss-Newton algorithm implemented by Simon Arridge and Martin Schweiger was used. The details of the reconstruction method are outside the scope of this thesis.

2.5 Simultaneous reconstruction of scattering and absorption

In clinical applications of optical tomography, the absorption coefficients at different wavelengths are the most useful quantities. If the absorption coefficient can be accurately imaged, it is possible to estimate [HbO_2], [Hb], and the oxygen saturation which is the ratio $[HbO_2]/([Hb] + [HbO_2])$.[28]

In order to image the absorption coefficient correctly, it is necessary to model the scattering in the tissue accurately. In highly scattering tissues governed by the diffusion approximation, it is possible to image both scattering and absorption explicitly if two types of measurements are made at each position: one which measures the attenuation of the light, and another which measures the time-of-flight of the photons through the tissue. In the frequency domain, the logarithm of amplitude ($\ln A$) and phase can be used for this purpose. To illustrate the situation, we study the case of a cylinder which is homogeneous

apart from a single cylindrical perturbation (Fig. 2). The 15 detectors are located in the plane containing the perturbation. The simulated phase difference and ln A difference between a cylindrical phantom with a single (absorbing or scattering) perturbation and a homogeneous phantom are given in Fig. 3.

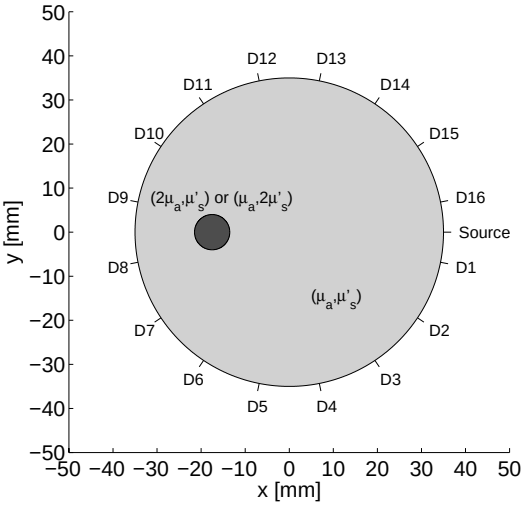

Figure 2. Cross-section of the imaginary cylindrical phantom used to illustrate the effects of a scattering or absorbing perturbation on the measured difference data between an inhomogeneous and a homogeneous phantom.

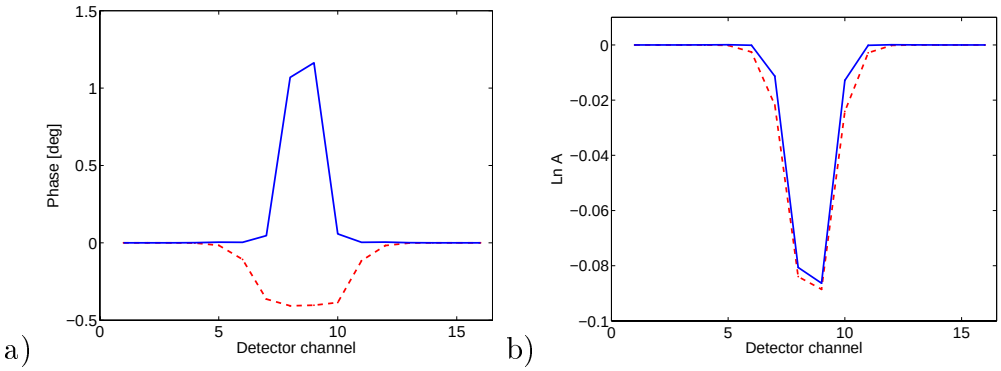

Figure 3. Effect of the absorbing (red '- -') and scattering (blue '–') perturbations on the simulated data. a) Phase, b) ln A.

It is evident from the graphs in Fig. 3 that both data types are necessary to distinguish between the two types of perturbations in the reconstruction as the difference in the effects of the two different types of perturbations on the amplitude is very small[62]. In addition, it can be seen that the effect of the absorbing object on the phase is broader than the effect of the scattering object on it. In general we can expect the spatial resolution of the scattering images to be better than that of the absorption images.

Using time-resolved measurements, Arridge and Hebden[46,63,64] have studied the reconstruction of scatter and absorption using the Mellin moments of the temporal point spread function (TPSF). The moments may be normalised to be independent of the absolute intensity, which makes the measurements less sensitive to the properties of the superficial layers of the tissue. However, it is difficult to obtain a sufficient number of photons to get adequate contrast-to-noise ratio for reconstruction using the higher-order moments. The amplitude and phase measurements from frequency-domain systems generally have a good contrast-to-noise ratio (CNR) and the practical reconstruction of scattering and absorption images is possible from either difference or absolute measurements[45,65].

As an example of a reconstruction of scattering and absorption from amplitude and phase measurement types, we study the case of a cylinder which is homogeneous apart from two perturbations in the central cross-section of the phantom [Fig. 8 (a) and (b) in Publication III]. The data was calculated using a 3D FEM solver for the DE and gaussian noise was added to the simulated data. In Fig. 4 (a) and (b) (Case I), the noise is only due to numerical errors (different meshes were used for the data generation and the reconstruction). In Fig. 4 (c) and (d) (Case II), the standard deviation of the added noise was 0.3° in phase and 0.015 in the logarithm of amplitude. In (e) and (f) (Case III), the noise was 0.5° in phase and 0.05 in the logarithm of amplitude.

The contrasts of the perturbations were $(2\mu_{a,bg},\mu'_{s,bg})$ and $(\mu_{a,bg},2\mu'_{s,bg})$ and the volume of each perturbation was 0.67 cm^3. The peak contrasts recovered in the reconstructions are given in Table 1. From the images, we can see that without noise, the perturbations are recovered with excellent image quality. In the presence of noise, the image quality deteriorates rapidly, and this is particularly evident in the contrasts of the reconstructed perturbations. The perturbations are so small and the scattering coefficient of the background so high that even in the noise-free case, the recovered contrast is only one-third of the true contrast. 16 sources and 16 detectors arranged in two rings are not enough for optimal contrast recovery.

Table 1. Contrast recovery in the presence of noise.

Property	Case I (noise-free)	Case II (moderate noise)	Case III (severe noise)
μ_a	25%	3%	N/A*
μ'_s	30%	13%	N/A*

* - perturbations were not adequately reconstructed

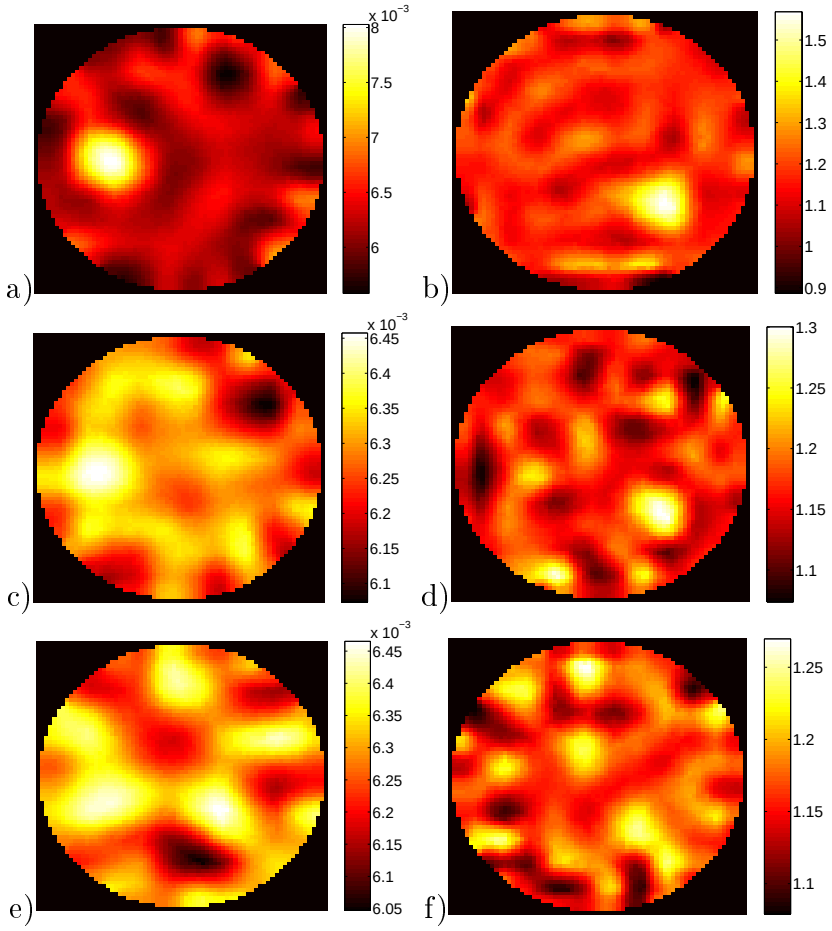

Figure 4. Reconstructed images from simulated data with different levels of noise. a) μ_a, b) μ_s' with no added noise; c) μ_a, d) μ_s' with $\sigma(\mathrm{n}_\phi) = 0.3°$ and $\sigma(\mathrm{n}_{\ln \mathrm{A}}) = 0.015$; e) μ_a, f) μ_s' with $\sigma(\mathrm{n}_\phi) = 0.5°$ and $\sigma(\mathrm{n}_{\ln \mathrm{A}}) = 0.05$. μ_a and μ_s' are in units of mm^{-1}.

2.6 Reconstruction of coupling coefficients together with the optical properties

In order to use the measurement of amplitude for optical tomography of the static properties of the tissue, it is necessary to consider the coupling of the light from the optical fibers to the tissue and vice versa. In the diffusion equation model, the source amplitude is usually specified to be 1, and the DE governs the decay of the amplitude as a function of increased distance from the source. Since the contact between the optical fibers and the tissue depends on the surface texture, the reflection and absorption characteristics of the skin, it is not easy to calibrate amplitude measurements so that they can be used directly in the reconstruction. In addition, while the diffusion equation correctly predicts the asymptotic behaviour of the amplitude as the distance grows, the absolute magnitude is different from Monte Carlo/RTE predictions, and the discrepancy depends on the optical

properties of the tissue under the optodes. Improvements in the source model have been suggested in the literature.[66,67]

Two approaches can be taken to solve the problem. In the first, the simulated data using homogeneous parameters and the measured data are compared. The model and measurement are fitted to match each other by changing the amplitude and phase coupling factors ($\ln A_c$ and $\ln \varphi_c$) between the model and measurement. The second approach involves an explicit reconstruction of $\ln A_c$ and φ_c together with $\mu_a(\mathbf{r})$ and $\mu_s'(\mathbf{r})$. This makes the reconstruction inherently non-unique.

If desired, the coupling coefficients for each source and detector fiber ($\ln A_{c,s}^{s}$ and $\varphi_{c,d}^{d}$) may be made free parameters in the reconstruction. This dramatically improves the quality of the reconstructions when hair is present between the skin and the optical fibers.[68,69] It may also improve the images if the radial positions of the optical fibers are not known precisely. If the tangential positions are inaccurate, additional free parameters are required in the reconstruction.[70]

2.7 Difference vs. absolute imaging

In absolute imaging, the measurements are carried out on the tissue and the reconstructions are generated directly using this data. The correspondence between the model and the physical situation must be almost exact because the variations in the measured quantities (φ and $\ln A$) due to the different source-detector distances are typically two orders of magnitude larger than the effects of the perturbations which need to be recognized in the images. The instrument developed by our group is the first which allows the simultaneous recovery of absorption and scatter in phantoms with tissue-like optical properties (premature infant's brain) and realistic target-to-background contrasts based on amplitude and phase without the use of a homogeneous reference phantom. To obtain absolute measurements, the instrument is first calibrated using a three-step procedure. Recalibration is generally needed after changes in the hardware.

Two different approaches to difference imaging are widely used. In the first, the background optical properties are assumed to be homogeneous, and the changes in the measured data due to a physiological change in the tissue are recorded by the instrument. These changes are used to generate images of the changes in the optical properties of the tissue. This procedure is easy to use but may produce inaccurate results because of the incorrect assumption of homogeneous background optical properties. In the second approach, a reference phantom with known optical properties and a similar geometry to the tissue is measured. The reference measurements are subtracted from the actual tissue measurements, and the differences in the measured data are used to generate the maps of optical properties in the tissue. Difference imaging does not require calibration (although errors

may be made depending on how accurately the optical properties of the reference state are known) and it is less demanding on the accuracy of the measurements. For these reasons, it is the most commonly used approach in experimental optical tomography.

In mammography, the breast can be immersed in a scattering liquid which fills the gap between the optical fibers and the breast. The liquid may be used as an easy-to-use reference phantom. In head applications, immersion cannot be used and the complex shape of the head makes the manufacture of a reference phantom for each subject difficult. In such cases, absolute imaging is more convenient.

The optical property distribution obtained with optical tomography may be useful for improving the quantitative accuracy of the imaging of physiological changes in the tissue during an activation experiment.

3 Optical activation imaging

3.1 General

Near-infrared spectroscopy has been extended to two-dimensional mapping (*optical topography*) of hemodynamic changes in the cerebral cortex due to brain activation using multichannel systems [9,11,15,27,39,71–74]. Model-based reconstruction techniques have not been widely used in activation studies due to the complexity of the optical structure of the head and the strong attenuation of light in the head. Prince et al.[75] applied a layered model of the head governed by the diffusion equation as the forward model and reconstructed the changes in the absorption in the motor cortex during a hand tapping task. They applied Kalman filtering to reconstruct images of time-varying signals. Klemer et al.[76] used the General Linear Model (GLM) and Principal Component Analysis (PCA) to analyze the time-series in the frontal and motor cortexes.

Instrumentation for activation imaging is generally optimized for a short image refresh rate. This allows the time course of the events to be studied almost simultaneously at each point in the imaged area. It can be implemented using fast time-multiplexing (pulsing) of the source fibers or by frequency-multiplexing. Frequency-multiplexing is a technique in which all the source fibers are active simultaneously and the light entering each source fiber is intensity modulated at a specific frequency, which allows the contributions from different sources to be identified by their frequencies in the detected signal.

The frequency-domain system developed by our group uses a PMT detector with a QE of approximately 8% at 800 nm. The SNR is sufficient for the application of the system in cortical activation studies. When a high temporal resolution is needed, the optical power of the light sources should be at least ten milliwatts. An advantage of the system is the phase measurement which can be used to estimate the pathlength in the modified Beer-Lambert law. If a light-propagation model is used, it is possible to use the calibrated amplitude and phase to estimate the optical properties of the surface layers which would probably improve the accuracy of the estimate of the concentration changes. For premature infant subjects whose head diameter is at most 90 mm, it is possible to do a tomographic measurement of the optical properties in the volume. Tomographic measurements of activation-related absorption changes require a dense array of sources and detectors over the area of interest, and ideally optodes should be placed on all sides of the head. The activation-related signals are fairly weak ($\Delta\mu_a \sim 10\%$) and transmittance measurements through a premature infant's head need to have a measurement time of at least 5-10 s per source position if we want to reliably detect localized absorption changes of that order of magnitude.

3.2 The modified Beer-Lambert law

To calculate changes in [HbO_2] and [Hb] in the tissue between the source and detector using measured changes in the attenuation of light at two wavelengths λ_1 and λ_2, the modified Beer-Lambert law can be used in the differential form:

$$\Delta \mathbf{c} = (\alpha^T \alpha)^{-1} \alpha^T \frac{\Delta \mathbf{A}}{d \times \mathrm{DPF}}, \tag{3}$$

in which $\Delta \mathbf{c}$ is a 2x1 vector containing the concentration changes of the two chromophores, α is a 2x2 matrix containing the specific extinction coefficients of the two chromophores at the wavelengths used, $\Delta \mathbf{A}$ is a 2x1 vector which contains the attenuation changes (in logarithmic units) at the two wavelengths, d is the distance between the source and detector fibers, and DPF is the diffuse pathlength factor.[77]

This approach assumes that the scattering of light is static, i.e., μ_s' stays constant over time, the optical properties of the background are homogeneous, and that the concentration changes occur globally in the tissue. In practice, these conditions are only met approximately in muscle and breast tissue, while the head is optically highly heterogeneous and a more sophisticated approach is needed to obtain quantitatively accurate results.

3.3 Modeling of the optical structure of the head

In order to improve the quantitative accuracy of activation imaging, a light-propagation model might be used with a linear inversion method to localize the hemodynamic changes. If an anatomical MR image set is available, it can be segmented into different tissue types and the optical properties of the outer layers (the scalp and the skull) can be determined from the optical phase and amplitude measurements[78]. The optical properties of the inner parts of the brain can probably not be determined reliably from optical tomographic data even in the presence of anatomical MRI data because of the effect of the CSF. The difference data from the optical activation measurements could be used together with a linear reconstruction method which uses the light-propagation model to generate cortically constrained activation maps. Monte Carlo methods have been used as the forward model in realistic models of the adult head[78,79]. A basic problem with these approaches is that the optical structure of the CSF area is not well understood, and the sensitivity of the measurements to the exact boundaries of the CSF is thought to be high[80]. A method for the determination of the optical properties of the head using the diffusion equation as the light-propagation model has been proposed by Barnett et al.[31]. An alternative to the Monte Carlo forward model is the solution of a higher-order diffusion equation[81] or RTE itself[82].

One of the many interesting applications of the realistic head model is the study of the dynamic processes in the superficial layers of the head and the gray matter of the brain.

From the practical viewpoint of the clinical and neuroscientific applications of NIRSI, it would be very useful to be able to separate these changes from each other based on measurements with sources and detectors on the same side of the tissue.

3.4 Hemodynamic studies of cortical activation in the literature

Responses in [HbO_2] and [Hb] to motor, somatosensory, visual, and auditory stimulation in adults have been published by several groups[83–98]. Simultaneous NIRS data with EEG[99] and fMRI[100–102] have been successfully recorded. Two groups have performed NIRS measurements with TMS and have recorded the hemodynamic response directly under the stimulation coil[103,104]. Studies of visual, olfactory, passive motor, somatosensory, and auditory responses have been carried out in infants[105–112].

4 Instrumentation

A comprehensive explanation of the intensity-modulated instrument designed in this thesis is given in Publications II and III [44,45]. The purpose of this narrative is to give background information on the principles behind the design of the system.

4.1 Detectors for optical tomography

Three types of detectors are available which perform well in near-infrared wavelengths and have sufficient dynamic range for practical use in optical tomography. Detectors based on silicon photodiodes (SiPD) have a peak sensitivity between 900 and 1000 nm, a high QE (typically 70-80%), and a large sensitive area ($\sim 10\,\mathrm{mm}^2$), but the temporal response of large-area photodiodes is not fast enough for RF modulation. Avalanche photodiodes (APDs) have a lower noise-equivalent power (NEP) of the order of $10\,\mathrm{fW}/\sqrt{\mathrm{Hz}}$ and a faster time response, allowing modulation at RF frequencies. However, APDs have additional noise introduced in the charge multiplication process, which is proportional to the square root of the photocurrent. SiPDs have better SNR at large intensities than APDs.

Photomultiplier tubes (PMTs) are manufactured with a variety of photocathode and window materials which affect the spectral sensitivity and noise characteristics of the detector. NIR sensitive types include metal cathode and GaAs PMTs. PMTs generally have a relatively large photosensitive surface and they maintain a bandwidth of hundreds of MHz depending on the model. PMTs have a relatively low QE in the near infrared, typically 1-10%. However, their NEP values are of the order of $0.1\ \mathrm{fW}/\sqrt{\mathrm{Hz}}$, which means that they offer excellent performance at low light levels.[113–115]

To illustrate the relative merits of four detector types, Fig. 5 shows the SNR of an APD (Hamamatsu S2384[116]), a SiPD with an integrated amplifier (Hamamatsu S5590[115]), the Hamamatsu H6780-20 room-temperature PMT module[114] and the corresponding cooled PMT module (H7422-20)[115] as a function of the optical power of the incident light at a wavelength of 800 nm.

The PMT and APD detectors are suitable for RF modulation, while the large-area SiPD is not. However, the popularity of SiPDs for activation measurements with pulsed light or IF modulation at relatively short source-detector distances is justified based on the performance of these detectors at incident optical powers of the order of 1 nW typically obtained in activation measurements with a 25 mm source-detector separation. In optical tomography, the transmissive measurements carried out with the source and detector on opposite sides of the tissue are the most important. In this case, the detected optical powers are typically of the order of 10 fW.

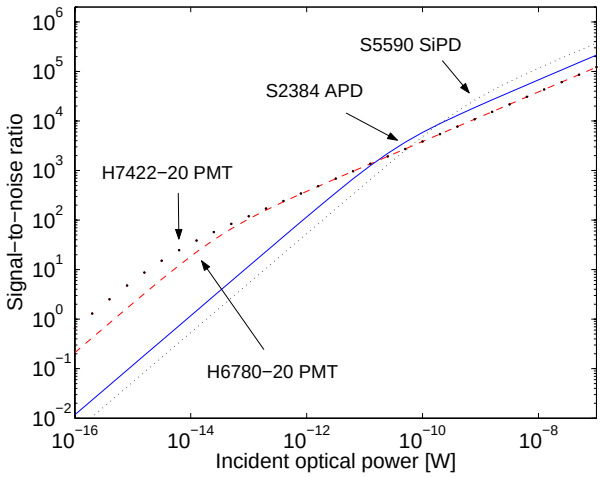

Figure 5. Theoretically predicted SNR of selected photodetectors as a function of optical power using a bandwidth of 1 Hz and a wavelength of 800 nm.

4.1.1 Noise in photodetectors

The RMS amplitude of the shot noise in the current of photoelectrons due to the random arrival of the photons is expressed as

$$I_{\text{photon}} = e\sqrt{2\eta I_p \Delta f}, \tag{4}$$

where e is the charge of the electron, η is the probability of photoelectron emission (QE), I_p is the photon arrival rate, and Δf is the bandwidth of the measurement.

At low photon rates, a second component known as the *dark current* becomes significant. This is due to spontaneous thermal exitations of electrons in the photosensitive material. It is independent of the incident optical power and is denoted I_{d} (all currents in this sections are RMS amplitudes). The noise current in the presence of dark current and the standard deviation of photon noise is expressed as

$$I_{N,SiPD} = \sqrt{I_{\text{photon}}^2 + I_{\text{d}}^2}. \tag{5}$$

In APDs, the internal gain mechanism causes additional noise, and we obtain

$$I_{N,APD} = \sqrt{I_{\text{photon}}^2 + I_{\text{d}}^2}\, M^{1+\chi/2}, \tag{6}$$

where χ is the *excess noise index*, typically 0.3 in the S2384, and M is the gain.[116,117]

In PMTs, the photoelectrons are multiplied by repeated acceleration and secondary emission. This process increases the noise of the anode current and its noise figure (NF) may be approximated using

$$\text{NF} \approx \frac{\delta}{\delta - 1}, \tag{7}$$

where δ is the secondary emission ratio at each dynode, which depends on the gain of the PMT. In this analysis, we use the value $\delta = 6$. The dark current of the PMT is usually expressed in the direct current (DC) form, which is converted into an alternating current (AC) expression using

$$I_{d,ac} = \sqrt{2eI_{d,dc}\,\mu\Delta f}, \tag{8}$$

where μ is the gain of the PMT.

The PMT noise may be expressed as

$$I_{N,PMT} \approx \sqrt{(\mu^2 I^2_{\text{photon}} + I^2_{d,ac})\,\text{NF}}. \tag{9}$$

In addition, PMTs have voltage and light hysteresis which cause the response of the detector to be delayed when a step change in light intensity or high voltage is applied. This effect is of the order of 0.2% of the relative change in anode current in the H6780-20 PMT.[113,114]

4.2 Measurement principle

In a frequency-domain optical imaging system, the intensity of the light source is modulated with a radiofrequency signal. A modulated light source can be thought to invoke diffuse photon density waves in the tissue studied[52,59,118–121]. If the light source is sinusoidally modulated, the intensity of the detected light is also sinusoidal with the same frequency but the amplitude is attenuated and the phase shifted from their values at the source position. The phase and amplitude of the photon density wave at the detection point are measured for each source-detector combination.

In a *homodyne* system, the phase and amplitude are measured directly at the (RF) modulation frequency. In a *heterodyne* system, the signal detected at the modulation frequency is mixed with a second RF signal and low-pass filtered to obtain a signal at an intermediate frequency (which has the phase of the original radiofrequency signal) before phase and amplitude detection. The heterodyne principle was used in this work.

4.2.1 The modulation frequency

The contrast-to-noise ratio of phase measurements at different modulation frequencies in the context of cortical activation studies in the reflection geometry was studied by Toronov et al.[122]. Through theoretical considerations and simulations, they concluded that the optimal phase CNR is obtained between 400 and 500 MHz when the source-detector separation is between 15 and 35 mm. At long distances between the source and detector, the high-frequency signals are attenuated strongly by the diffusion of light and to prevent the decay of the signal, a frequency between 100 and 200 MHz is appropriate. The

effect of modulation frequency on the quantification and localization accuracy of scattering or absorbing perturbations in a homogeneous background was studied by Boas et al.[52]

Frequencies up to ~ 200 MHz are relatively easy to implement with a wide dynamic range, as the power splitters and mixers have excellent isolation characteristics (~ 65 dB) up to that frequency. The temporal accuracy of our system is limited by drift in the optical components (PMT and laser diode) and photon shot noise instead of the internal stability and noise of the RF system at the modulation frequencies tested (100 MHz and 450 MHz). The temporal precision of the RF system without the optoelectronics is of the order of 0.01° at 100 MHz.[44] A modulation frequency of 100.0427 MHz was used in the multichannel measurements.

4.2.2 Phase and amplitude detection

The IF signal from the receiving mixer is low-pass filtered, amplified, and digitized at 20 kHz using a multichannel ADC card in the differential input configuration. The raw data from two synchronized multichannel ADC cards are written directly to a hard drive and the phase and amplitude signals are calculated after the actual measurement using a software lock-in amplifier (LIA).

In a digital LIA, the digitized input signal is multiplied in turn by sine and cosine reference waveforms. These intermediate signals are then low-pass filtered to obtain the X and Y signals.

$$X(t) = b(0)s(t)\sin(\omega t) + \sum_{i=1}^{3}\left[b(i)s(t-i\Delta T)\sin(\omega(t-i\Delta T)) - a(i)X(t-i\Delta T)\right], \quad (10)$$

$$Y(t) = b(0)s(t)\cos(\omega t) + \sum_{i=1}^{3}\left[b(i)s(t-i\Delta T)\cos(\omega(t-i\Delta T)) - a(i)X(t-i\Delta T)\right], \quad (11)$$

where $a(i)$ and $b(i)$ are the IIR filter coefficients ($i = 0, 1, 2, 3$), ω is the angular frequency of the reference signal, and ΔT is the reciprocal of the sampling frequency. The phase and amplitude are calculated from X and Y using

$$A(t) = \sqrt{X(t)^2 + Y(t)^2}, \quad (12)$$

$$\varphi(t) = \arctan2\left(Y(t), X(t)\right), \quad (13)$$

where $\arctan2(Y, X) \in [-\pi, \pi]$ is a four-quadrant arcus tangent function.

The reference frequency (5 kHz) is generated using a programmable counter on the primary ADC card and it must be an integral fraction of the sampling frequency (20 kHz) and the main clock frequency of the card (20 MHz). The second card receives the clock signal from the primary card through the RTSI bus. The start of the data acquisition is timed by the primary card.

4.2.3 Amplitude and phase noise

Amplitude and phase noise are closely related to the noise in the intensity and mean time measurements in a time-domain system. Amplitude has the advantage over DC intensity that $1/f$ noise is reduced in the measurement bandwidth due to the high modulation frequency. A modulated signal is quite insensitive to cross-talk from signals carrying timing information such as trigger pulses. Because it is not safe to use 100% modulation of a laser diode as a reverse voltage can break the laser diode, a modulation fraction of approximately 80% is typically used in practice. In this case, 20% of the light entering the tissue does not carry the RF signal which is detected and measured, but it does contribute to the photon shot noise within the measurement bandwidth. In addition, the ratio of the modulated and the DC component of the signal decreases as the distance between the source and detector increases, especially at frequencies close to and above 1 GHz.

Phase noise consists of three components: the first is due to the imperfect synchronization of the modulation signal with the reference waveform generated by the ADC card, the second is due the random arrival times of the detected photons, and the third is due to the dark current. In our system, the first component exists mainly as a slight phase drift while most of the higher-frequency noise in the phase is due to photon shot noise or the dark current. Phase has a smaller CNR for absorption changes in the tissue than amplitude, but the ratio of its sensitivity to changes in the internal parts of the tissue to changes on the surface is also smaller, which makes the measurements more reliable in the presence of hair. To obtain adequate CNR for phase, the optical power of the detected light should be as high as possible.

4.3 Dynamic range

In 1998, Chance et al.[42] and Ramanujam et al.[43] described the state of the art in phase and amplitude measurement systems of that time and highlighted their problems. Amplitude measurements are largely unaffected by the high modulation frequency, except for the existence of radiofrequency coupling between the source and detector electronics. In 2001, McBride et al.[41] published the first genuinely parallel optical tomography system using RF modulation. The amplitude measurement was found to be linear down to a detected optical power of 100 fW. Lower amplitude levels could not be measured due to the system noise floor. Phase noise was quite significant in this optical power range (15° at 1 pW with a measurement time of 2 s per source). The dynamic range of the system is adequate for optical mammography using high-power laser diodes, but the attenuations encountered in optical tomography of the head are much larger. Thus, the dynamic range and SNR need to be optimized for measurements at low light levels.

In time-domain systems, photon-counting techniques are used and the low end of the

dynamic range is limited by the dark count of the detector. The dark count is the number of photoelectron trains that are produced by the detector in a given time that are *not* caused by photoelectric emission on the photocathode. The electrons may be thermal or excited by cosmic rays. Some of these electron trains have different pulse heights than normal photoelectron trains so that they may be rejected by the photon counting electronics. In order to maximize the benefits of photon counting, it is necessary to cool the photomultiplier tube to reduce the dark count. Currently used photon counting electronics limit the high end of the dynamic range. State-of-the-art photon counting cards by Becker & Hickl allow the counting of several million photons per second, which corresponds to a detected optical power of the order of 10 pW (4% QE). In optical tomography, higher optical powers are encountered at short source-detector separations. In order to carry out a measurement in this case as well as in the long-distance case, variable optical attenuators (VOAs) may be used[64,123]. This technique involves the use of a rotating disc which contains holes of different sizes or, alternatively, neutral density (ND) filters of different densities. ND filters have a larger back-reflected component of light, which may cause an intensity-dependent measurement error in the temporal data types. However, they provide reproducible attenuation of intensity. The holes have the advantage of a smaller reflected component, making it easier to measure temporal data types accurately. However, the disadvantage is that the intensity is very sensitive to small random positioning errors of the VOA disc.

Modulated DC systems based on SiPD detectors have excellent performance at short and medium distances, but in order to obtain good results in transmission measurements, it is necessary to use PMTs, which reduces the SNR at short distances closer to that of frequency- and time-domain systems.

4.3.1 Detection of low light in the frequency-domain system

In the frequency-domain system developed in this thesis, the coupling of the RF signal between the light modulation electronics and the detection electronics was minimized to increase the dynamic range. Intricate RF shielding was developed to enclose all parts of the RF system. In addition to the aluminium enclosures, it was necessary to prevent internal leaking of the main modulating signal through the signal lines by using a carefully balanced chain of amplifiers, attenuators, and mixers to obtain the appropriate RF power levels and the necessary blocking of the unwanted modulating signal from the input of the mixer which converts the detected RF signal into the 5 kHz IF signal for the lock-in amplifier.

Two effects arise if the shielding is insufficient. Firstly, amplitudes much smaller than the leak signal will be invisible. Secondly, the leak signal generally has a relatively stable phase, and it is superposed on the true signal, causing the phase to distorted. This can be

seen as phase-amplitude crosstalk at low intensities and has been discussed by Alford and Wickramasinghe[124]. Interchannel crosstalk, if it exists, has similar effects on the phase and amplitude. In the current implementation of the instrument, the RF leak signal and interchannel crosstalk are significantly smaller than the noise level caused by the PMT dark current and the RF amplifiers. The detection limit of the system is currently of the order of $1\,\mathrm{fW}/\sqrt{\mathrm{Hz}}$. The dark current and detection limit of the system may be reduced further by a factor of 10 if a RF shielded and cooled photomultiplier tube is used. The disadvantage of cooling is the increased system cost and complexity.

4.3.2 Measurement of amplitude and phase at high intensities

A common problem in RF intensity-modulated systems is that the measured phase is distorted by a phase shift which is a function of the amplitude. The main cause of this phenomenon is the current-dependent redistribution of the high voltages which accelerate the electrons in the dynode chain. The dynode chain of a typical PMT is illustrated in Fig. 6.

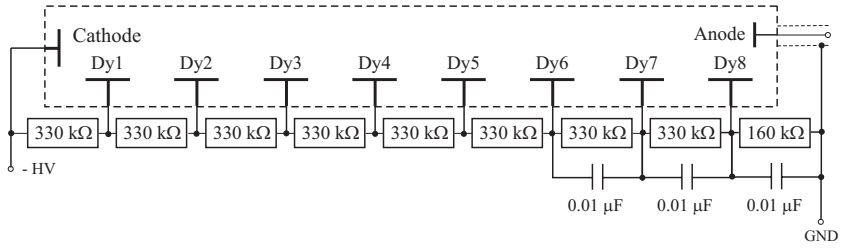

Figure 6. The dynodes of the R7400U PMT and a voltage divider circuit.[113]

The high voltage applied between the last dynode (anode) and the photosensitive cathode is divided into several smaller high voltages (tens of volts each) by a voltage divider, which is a resistor network augmented by capacitors in parallel with the resistors for the last dynode pairs. The purpose of the capacitors is to allow the rapid release of electrons needed to generate the photoelectron pulse. During the time between the pulses, the capacitors are re-charged by the high voltage supply. The system works very well when the photocathode is exposed to relatively small light intensities. When the photocathode is totally blocked from light, very few electrons travel through the vacuum. The current that goes through the resistors in the voltage divider when the cathode is not exposed to light is called the quiescent current i_q. The current through the last resistor in the chain is reduced when the photocathode is exposed to light. The preceding dynode pairs are affected less and less by this change. If the decrease in current is large compared with i_q, a redistribution of high voltages in the resistor chain takes place according to Kirchhoff's and Ohm's laws. The high voltages accelerate the electrons of the photoelectron pulse through

the vacuum and changes in the voltages affect the times-of-flight of the electrons through the vacuum, and the phase of the signal carried by these electrons is changed. In order to minimize the distortion of phase, it is necessary to limit the anode current used in the measurements. In our system, it was found that phase-amplitude crosstalk was negligible if the anode currents were kept below 80 nA.

In order to realize the required dynamic range in optical tomography, it is necessary to adjust the high voltage of the PMT for each source-detector combination depending on the attenuation encountered during the measurement sequence. In the system reported by McBride et al.[41], the gains of each detector are adjusted before the measurement to an appropriate level. Each detector receives light from the fiber bundle which is at a fixed position relative to the source on the tissue surface. In this way, the effects of voltage hysteresis are reduced. However, the implementation requires coupling of the light between two fiber bundles which results in light loss and may affect the reproducibility of the measurements. In the DC implementation by Schmitz et al.[35], a multichannel PC-controlled variable gain IF amplifier is used instead of a direct adjustment of the detector gain. This technique by itself is not sufficient in our system as the phase-amplitude crosstalk and the dark current would limit the dynamic range.

It is generally known that when the incident light level or gain is changed, the signal from the PMT exhibits hysteresis. In the case of the H6780-20 PMT module, the anode current overshoots after a step increase in light level. If the incident light is held constant after the step change, the anode signal returns to a lower steady-state value by following an exponential decay function. The effects of light hysteresis in the H6780-20 have practical significance in optical tomography when the incident optical power is above 1 nW, which corresponds to the shortest source-detector distances ($1-2$ cm) used in practice. At these distances, the measurement accuracy is limited by hysteresis instead of photon shot noise. If the source fibers are ordered in such a way that the adjacent channels in the switching order are positioned close to each other on the surface of the tissue, the effects of hysteresis and interchannel crosstalk are minimized.

The PMT module used in the instrument has a 200-ms settling time when the gain is adjusted. No obvious voltage hysteresis has been observed after this period. The approach chosen has proven to give very good repeatability of the tomographic measurements provided that the switching order is kept constant during the measurement. Randomized or counterbalanced switching may be used to reduce the effects of the system drift and physiological changes in the tissue during the relatively slow tomographic measurements. However, varying the switching order reduces the reproducibility of the measurements due to the effects of hysteresis in the PMTs and in the optical switches.

4.4 Noise and measurement time

The practical sensitivity of phase and amplitude measurements to hemodynamic changes in the cortical tissue were investigated. The measurements were performed on adults with visual and motor stimulation. Stimulus-correlated amplitude changes were found in a greater proportion of the studies than phase changes, but the phase changes which did occur were better localised than the amplitude changes. However, phase changes can not be converted into concentration changes in a straightforward way as is the case with amplitude changes. Amplitude measurements have sufficient sensitivity for changes in the cortex even when a higher temporal resolution or a low source power is used. At present, the image refresh rate of our system is limited by the DiCon VX500 switch, which has a switching time betwen 300 and 556 ms. We plan to replace it with a MEMS switch which has a 2-ms switching time but inferior interchannel isolation.

The short-term reproducibility of the system in a tomographic measurement was investigated in Publication IV. A homogeneous cylindrical phantom with a diameter of 70 mm and optical properties of $\mu_s' \approx 1\,\mathrm{mm}^{-1}$ and $\mu_\mathrm{a} \approx 0.01\,\mathrm{mm}^{-1}$ was measured repeatedly for six times using a source power of 8 mW and a measurement time per source of 5 s. The mean standard deviations of phase and $\ln \mathrm{A}$ over the repeated trials were 0.08° and 0.004, respectively.

4.5 Stability

For quantitative measurements of phase and amplitude, it is necessary to optimize the stability of the system. The radiofrequency system was stabilized using a technique called phase-locking in which the frequencies of the primary and secondary RF signal generators are locked to each other so that their difference frequency stays in phase-lock with the reference signal generated by the analog-to-digital converter card. The performance of the RF system in a closed loop without the optics was studied in Publication II.

Several componenents in the RF system were found to cause phase drift if their temperatures were allowed to raise. Heat sinks were attached on the RF amplifiers, splitters, and mixers to reduce thermal fluctuations in the phase.

The laser diode temperature is a major potential source of instability in the system. Therefore, a temperature stabilization system was developed for the laser diode. The temperature of the NTC resistor which is placed in contact with the laser diode can be controlled between 20 and 30° C to a precision of $\sim 1\,\mathrm{mK}$. The laser diode mount was designed to minimize RF cross-talk between the laser diode electronics and the other parts of the system.

4.6 Compromises made in the instrument design

An ideal optical tomography system would produce data with little noise and minimal systematic errors, yet feature a wide optical dynamic range and a short imaging time. In a practical implementation, a trade-off between these characteristics needs to be made.

The light sources used in intensity-modulated systems are usually laser diodes, as they produce nearly monochromatic light, they are available at low cost, and they can be easily modulated using the injection current. At an early point, we noticed that the stability of the light from the laser diodes was insufficient for optical tomography if the temperatures of the laser diodes were not tightly regulated. Thus, we opted to use a single laser diode for each wavelength used, and time-multiplexing using a switch was used to select the active source fiber and deliver the light to it according to a user-defined sequence.

In most cases, the distance from the source to the detector position in cortical activation imaging should be approximately 30 mm. This is a compromise between obtaining a good SNR and contrast for the cortical parts of the brain. If the detector is placed further away, the SNR is reduced by a factor of 3 for each 10 mm increase in separation, and the sensitivity of the measurement is spread over a larger volume in tissue. On the other hand, if the distance is decreased below 25 mm, the sensitivity of the measurements to changes in the superficial layers such as the skin and skull increases and the sensitivity to changes in the brain decreases.

In systems optimized for cortical activation imaging, several groups have chosen a more time-efficient approach.[19,20,27] Instead of having one source fiber active at a time, several or all of the sources illuminate the tissue simultaneously, which allows the rapid collection of data from a large area of the cortex. This is made possible by the fact that most optode layouts designed for optical activation imaging are designed so that only the data for a single source-detector distance is used to generate the two-dimensional images. Thus, the dynamic range requirements of the system are very modest. Several sources far apart can be active simultaneously in a pulsed system as long as the distance is sufficient to guarantee isolation. In a frequency-multiplexed system, the light sources are modulated at different frequencies. This method has the advantage that the time resolution is excellent since the data can be collected simultaneously for all the sources and detectors, but the disadvantage is that a separate laser diode and lock-in amplifier or equivalent amplitude detector are required for each combination of source position and wavelength. The systems are usually operated at an image refresh rate of the order of 200 ms.[19,20,27]

In the current implementation, the gain switching is implemented using the high-voltage supply in the PMT module. The settling time is 200 ms, which can be reduced to 50 ms by replacing the module with a separate PMT and an external high voltage supply. Another way to improve switching speed is to use progammable IF amplifiers.

The light collection efficiency of the detecting bundles is compromised by the numerical aperture (NA) of the fibers, which is currently 0.22. Several times better collection efficiency could be obtained by using optical fibers with a larger NA but the amplitude and phase would be more sensitive to bending of the optical fibers.

The H6780-20 photosensor module has an integrated voltage divider circuit, the details of which are proprietary information. The 80-nA upper limit for the anode current may be increased by reducing the resistances of the voltage divider circuit, which has the effect of increasing i_{q}. This requires a high voltage supply which can deliver a larger current. Increased i_{q} has the benefit of allowing the PMT to be used at a higher gain, which improves the SNR of the light detection system particularly when the detected optical power is relatively high. However, operating the PMT at large anode currents might cause a reduction in its lifetime.

4.7 Calibration

A three-step calibration procedure was implemented. The first step consists of the determination of the sensitivity of the measured phase and amplitude to changes in the high voltages applied to the PMTs. The gain characteristics of each detector are measured separately[45]. The second step consists of the determination of the relative differences between the attenuations and phase shifts of the different source and detector channels[48]. The third step consists of the measurement of the phase and amplitude of the absolute calibration tool using one source and one detector channel[44]. A detailed description of the procedure is given in Publication III.

4.8 Patient interface

In measurements of the arm, the adult head, and the neonatal head, the optical fibers were attached to the surface of the tissue using a low-temperature thermoplastic material made by WFR/Aquaplast Corp. Aquaplast can be shaped to fit the tissue by heating it in 75-degree (C) water. The procedure is quick and patient-friendly. Two types of sleeves were used (Fig. 7); the first allows the mounting of the optical fibers in contact with the surface of the skin, and the second allows the mounting of the fibers so that they are stopped at a short distance (2 mm) above the skin. We found the latter easier to use in many ways, as it doesn't distort the shape of the tissue and it prevents the fibers from denting the skin. However, the contact mount allows the hair to be moved aside from under the optical fibers by removing the inner sleeve so that the attenuation and also the effects of hair movement are reduced. In general, it is difficult to obtain good measurements on subjects with dark hair. The illumination and detection areas need to be relatively large, as this reduces the heating of the skin and allows larger optical powers to be used. Also, variations in the

surface texture and characteristics are averaged over a larger area, giving more reliable measurements of the internal properties.

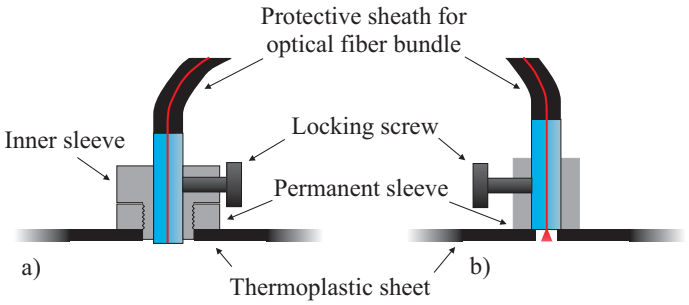

Figure 7. Fiber mounting sleeves. a) Adult contact, b) neonatal non-contact type.

5 Optical tomography of tissue-equivalent phantoms

Several tissue-equivalent cylindrical phantoms were made of polyester resin. The resin is clear by itself, but TiO_2 particles and a NIR dye are added to the mixture during the manufacturing process to mimic the scattering and absorption properties of tissue. The index of refraction of the resin is 1.56 and the forward-scattering anisotropy of the TiO_2 particles is $g \approx 0.5$. The phantoms are hardened during the manufacturing process as this makes them durable so that measurements can be repeated.[125]

One of the phantoms has two embedded objects, one with twice the background scattering, and another which has twice the background absorption. The volumes of the two objects were $0.67\,\mathrm{cm}^3$ each and they were located in the central cross-section of the phantom. The background optical properties were similar to those in the head of premature newborn infants ($\mu_\mathrm{a} \approx 0.01\,\mathrm{mm}^{-1}$ and $\mu_\mathrm{s}' \approx 1\,\mathrm{mm}^{-1}$) at 800 nm.

The instrument was first calibrated according to the method described in detail in Publication III. The optical fiber bundles were attached to the surface of the phantom in two rings; eight sources and eight detectors in each ring. The positions of the targets and the optical fiber bundles are illustrated in Fig. 8.

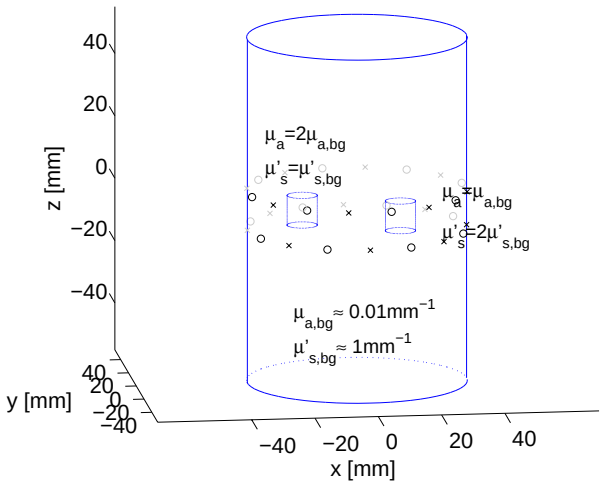

Figure 8. The cylindrical phantom with two embedded objects. The source positions are indicated with crosses and the detector positions with circles.

A regularized Gauss-Newton algorithm was used to make images of μ_a and μ_s'. Slices of the reconstructed images in the xy plane and the xz planes through the objects are shown in Fig. 9. The novelty in these results is that the calibration is independent on the light propagation model. The modeling and measurement errors affect the example phantom reconstruction as much as they would in a reconstruction of a tissue or phantom having an arbitrary geometry.

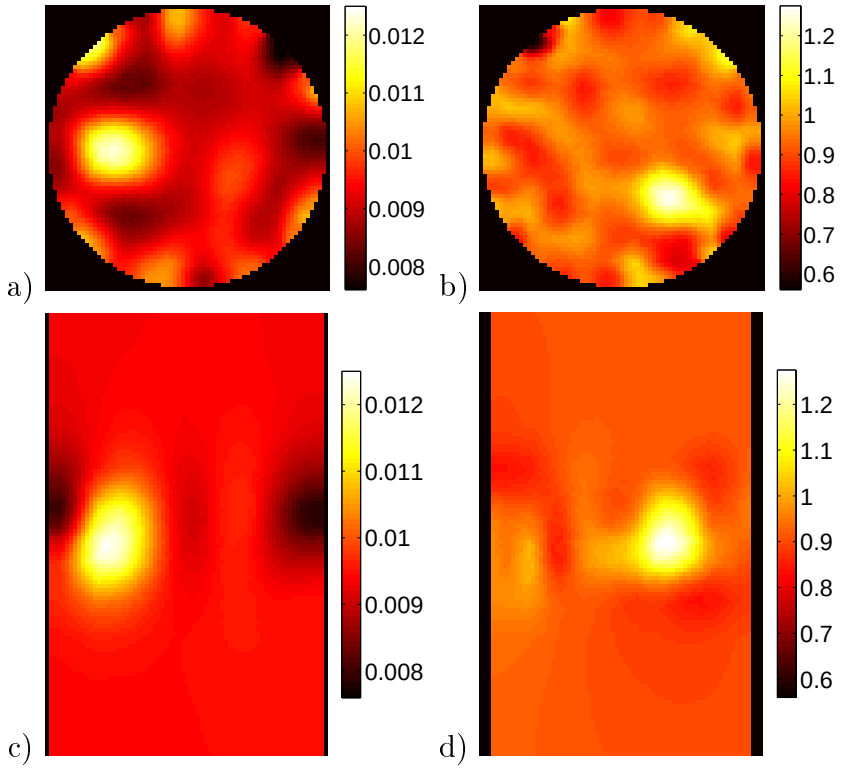

Figure 9. Images reconstructed from measured and calibrated data. a) μ_a at $z = 0$, b) μ_s' at $z = 0$, c) μ_a at $y = 0$, and d) μ_s' at y = -12.24 mm. μ_a and μ_s' are in units of mm^{-1}.

The parameters and geometry of the phantom are the same which were used to generate the simulated data for the reconstructions in Fig. 4 in Sect. 2.5. In addition to absolute images, images of similar quality reconstructed from difference data measured with various imaging times are shown in Publication IV, together with a quantitative analysis of the image quality.

6 Activation imaging using the system

6.1 Measurement of interhemispheric connections using TMS and NIRSI

In traditional neuroimaging paradigms, an imaging modality such as MEG, EEG, or fMRI is used to record the indirect effects of neuronal activity by measuring the electrical potentials (EEG) and magnetic fields (MEG) on the surface of the head, or changes in the concentrations of deoxyhemoglobin (the blood oxygenation level dependent contrast or BOLD) inside the brain (fMRI). Changes in the neuronal activity are triggered by having the subject perform a task or by letting the subject sense timed stimuli. The activation patterns of the brain are then recorded using the neuroimaging method. Visual, somatosensory, and auditory tasks are frequently used. A relatively new stimulation method is transcranial magnetic stimulation (TMS)[126] which allows the direct activation of cortical neurons non-invasively, without opening the skull. TMS has been used together with EEG in several studies[127,128]. The method allows the imaging of neuronal activation patters with a millisecond temporal resolution. The combination of near-infrared spectroscopic imaging (NIRSI) with TMS is an interesting possibility which allows the hemodynamic responses induced by TMS to be studied with relatively inexpensive instrumentation. The method may be used to study cortical reactivity and transcallosal connectivity.

In this study, four volunteers were studied with a four-channel (5 source positions, 4 detectors) implementation of the system. TMS was applied to the left motor cortex [see Fig. 10], and the optical fibers were attached in a rectangular grid on the right hemisphere over the assumed location of the motor cortex. The measurements were carried out with a wavelength of 830 nm, which is mainly sensitive to changes in [HbO_2]. [Publication V]

Figure 10. Measurement setup for TMS and optical imaging.

In response to TMS, we observed a decrease of amplitude at 830 nm of the order of 1% in the motor cortex, and an increase in the amplitude in premotor areas anterior to the right motor cortex. The somatosensory area of the hand in the right hemisphere was localized using magnetoencephalography (MEG) and left median nerve stimulation. In Fig. 11, the change in amplitude at 830 nm is displayed as a two-dimensional interpolated map. In this figure, the location of the N23m MEG dipole has been projected onto the surface of the brain (white dot).

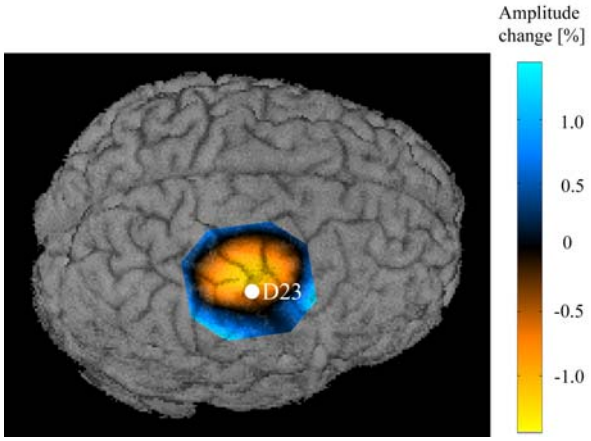

Figure 11. Interpolated difference image showing the change in amplitude during stimulation vs. rest. D23 is the projected position of the MEG dipole at t = 23 ms after the onset of the stimulus.

The time course of the amplitude in an activated area as well as the time course in the premotor area where the brain is thought to be deactivated due to transcallosal inhibition are shown in Fig. 12. Notice that changes in regional CBF or [HbO_2] do not automatically indicate a change in neuronal activity, but the correlation between the stimulation cycle and the measured amplitude is a reasonable indicator of stimulus-related changes in neuronal activity. Changes in the global circulation may be phase-locked with the stimuli, which suggests that it is a good idea to follow systemic changes during an experiment.

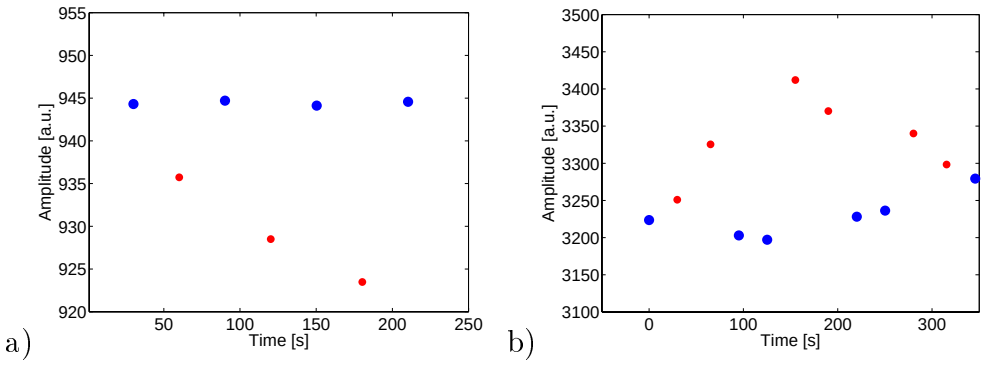

Figure 12. Time course of the TMS-induced amplitude changes. a) Activated area, b) deactivated premotor area. The small red dots were measured during TMS, and the large blue dots were obtained during the rest periods.

Optical imaging during TMS was found to be challenging because the stimulation coil could move slightly with respect to the head during the experiment, causing hair movement and sometimes a displacement of the optical fibers. Before the measurements, the hair between the optical fibers and the skin was moved aside as far as possible using compressed air. A vacuum pillow was used to support the head, and the stimulation coil was mounted on a camera support arm attached to the chair. Nevertheless, the subjects were adults with relatively long hair, and several measurements had severe motion artifacts.

The imaging paradigm consisted of ten interleaved 30-s periods of rest and stimulation. During each stimulation period, 15 TMS pulses were applied at 2-s inter-stimulus intervals. The optical imaging was timed so that the transition between the stimulation and rest periods triggered a 5-s pause in the imaging followed by the sequential illumination of each source fiber for 5 s in turn. The relatively slow switching interval was selected in order to minimize the effect of the dead time on the SNR of the phase measurements. Phase changes have a relatively high sensitivity to changes in the cortex vs. the skin, and therefore they are less sensitive to the effects of hair movement during the experiment than amplitude changes. In the measurements with magnetic stimulation, a significant correlation between phase and the magnetic stimulation was found in only a few measurements, despite our efforts to minimize phase noise in the instrument design. The location of the significant phase changes in the TMS experiments was in the lower-right corner of the imaged area. This finding supports the idea of transcallosal inhibition of the right premotor areas when the left primary motor cortex is stimulated with TMS. However, a simple concept such as the modified Beer-Lambert law cannot be used to determine concentration changes from phase data. Instead, a realistic optical model of the head should be used. If only amplitude data are used, it is reasonable to use a fast image refresh rate because amplitude measurements have a relatively high CNR even with short measurement times.

In conclusion, both increases and decreases of the 830 nm amplitude signal were observed in areas in and around the motor cortex using optical imaging. The increase in amplitude in the premotor area was statistically significant in almost all the measurements with TMS. While in most cases the 830 nm amplitude decreased in the primary motor cortex (M1), it was statistically significant only in four measurements out of ten. It appears that the initial reaction after the onset of stimulation is deactivation in both M1 and the premotor cortex, but the response in M1 changes to activation during extended stimulation, giving finally an overall decrease of amplitude during the stimulation periods vs. rest. In Fig. 12 a), the response is seen to increase towards the later stimulation periods. The responses induced by TMS are complex and in order to understand them correctly, sequences with different timing of the rest and stimulation periods, different inter-stimulus intervals, and different TMS pulse intensities need to be used and their effects studied. Subjects with short and light hair should be chosen as the probability of statistically significant responses from subjects with long and dark hair is very low.

6.2 Optical imaging of hemodynamic responses in the neonatal auditory cortices

In order to study the viability of using optical imaging as a tool for neonatal activation studies, we performed a series of measurements with the 16-channel dual-wavelength system. Auditory measurements on both hemispheres, visual measurements on the occipital cortex, and somatosensory experiments were carried out. In Publication VI, we have outlined the first results of the bilateral auditory recordings.

In this study, we took advantage of the 16 parallel detection channels and used only two source fibers (one on each side of the head) in order to maximize the temporal resolution and still obtain enough data to locate the hemodynamic change above the ear. Eight detector fiber bundles were placed at a distance of 25 mm from the source fiber on each side (Fig. 13). Two of the detector fiber bundles were placed on the cheeks to obtain a reference measurement which is not sensitive to changes in the absorption in the brain. It was used to verify that what is recorded by the other channels is a local change in the CBF of the brain, instead of a stimulus-gated global hemodynamic change.

Figure 13. The auditory imaging experiment.

In Fig. 14, the neonatal auditory response to a sequence of seven beeps is shown as the base 10 logarithm of amplitude ($\log_{10}$A) with the baseline set to zero. The measurement wavelengths were 760 nm (blue curve) and 830 nm (red curve). The data has been averaged over 17 subjects.

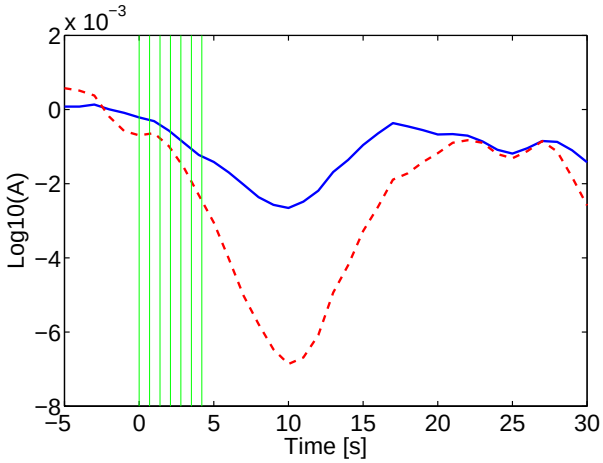

Figure 14. Time-course of the auditory hemodynamic response in $\log_{10}$ A *as a change from the baseline. The 760 nm data is shown by the solid blue line and the 830 nm data by the dashed red line. The green vertical lines indicate the onset of each auditory stimulus.*

For Fig. 15, the $\log_{10}$ A time-series were converted into Δ[Hb] and Δ[HbO_2] using the modified Beer-Lambert law.

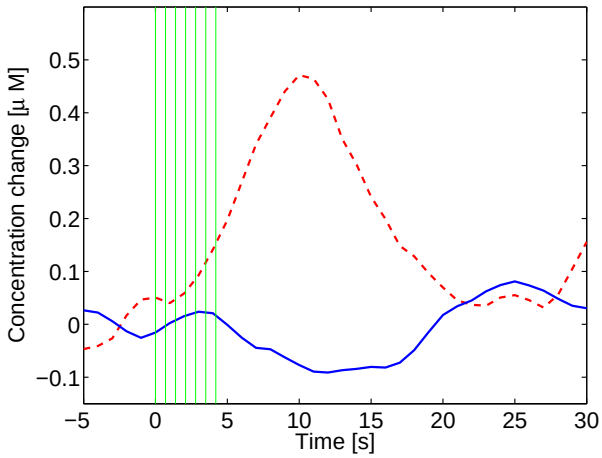

Figure 15. Time-course of the auditory hemodynamic response averaged over the right auditory cortices of 17 neonates. The solid blue curve depicts [Hb], the dashed red curve [HbO_2].

Although hemodynamic signals measured with diffuse light have modest spatiotemporal resolution, the temporal characteristics of the response may still provide new information on how the brain works and develops. For example, we discovered that the peak latency of the [HbO_2] time course is negatively correlated with the gestational age of the child.[129]

The optimal response to the beep stimulus is obtained by placing the optical fibers above the ear. A full-head helmet which was designed for premature infants has 32 fiber holders which can be moved in- and outwards to match the shape and size of the head. The helmet is designed so that basic auditory responses can be recorded. The current spatial density of optical fibers in the helmet is insufficient for cortical mapping, but it is likely that at least some visual, somatosensory, and auditive tests can be carried out with the same helmet which is used for tomography.

7 Conclusions

In this thesis, a frequency-domain optical tomography system was designed and implemented. The characterics and performance of the system were studied and described in detail in the publications. The system was successfully applied to generate images of small perturbations with moderate contrast in highly scattering tissue-equivalent phantoms. The ability to distinguish between scatter and absorption was confirmed.

In practical studies, an early 4-channel version of the system was used to study hemodynamic responses induced by TMS and transcallosal connectivity of the motor cortex. The 16-channel system was applied to bilateral imaging of hemodynamic changes due to auditory stimulation in full-term neonates.

In its current form, the system is suitable for optical tomography of the forearm, the premature infant's head, and if a suitable patient interface is developed, optical mammography. As a frequency-domain system, it is ideal for applications where both operational speed and quantitative results are desired. The switching time currently limits the data-acquisition rate so that the fastest rhythms of the body such as the heart beat can not be studied very well. The slower rhythms of the body such as the autoregulation of the circulation have a significant effect on the data. Kalman filtering and a model of the dynamic processes may be used to improve the results in physiological studies.[75]

The low-light sensitivity of the system may be improved by a factor of 10 (in terms of NEP) by using cooled PMT modules. A larger number of channels would increase the recovered contrast in absorption and scatter and improve the spatial resolution of the system.

The main advantages of the system are its quantitative accuracy and optical dynamic range. The low-light detection limit of the system allows the study of thicker and more absorbing tissues than is currently possible with other frequency-domain or DC systems. The accuracy of the system has been demonstrated in phantom measurements which show that the μ_a and μ_s' distributions can be imaged with comparable quality using either difference or absolute imaging. Absolute imaging is useful in situations where a high-quality reference phantom is not available, such as in the optical tomography of premature infants, provided that adequate sensitivity can be obtained.

During the past five years, optical imaging has been demonstrated to be useful for the study of hemodynamic and metabolic processes in the arm muscles, the cortical activation imaging of adults and infants, the imaging of the brains of premature infants, and mammography. I think that optical tomography in its present form is a very interesting research tool and it can provide a wealth of information about the physiology of tissue in all of these fields. To me, the most interesting applications are those related to infants. In this work, I have tried to improve the quantitative accuracy of optical tomographic measurements to the next level. Future improvements in optical tomography are likely to come from

techniques which improve the accuracy of the registration of the optode positions and new reconstruction algorithms which partially compensate the effects of hair[69] and the lack of precise knowledge of the optode positions[70]. Improvements in the technology for imaging of the hemodynamic responses to cortical activation will include faster imaging times, algorithms which reduce the effects of hair movement, realistic models of the optical structure of the head, and increases in the spatial resolution of cortical mapping using overlapped grids.

8 Summary of publications

Publication I

This book chapter is a review of diffuse optical imaging. The article describes the interaction between NIR light and tissue, modeling the light propagation, methods for image reconstruction, instrumentation, and applications.

Publication II

In this paper, the single-channel version of the intensity modulated optical tomography system developed by the authors is discussed in detail. The performance of the electronics and the optics are described, and techniques for calibration of the data are suggested. The calibrated data is compared with a FE DE solution in the case of a cylindrical phantom.

Publication III

The multichannel implementation of the instrument is described. A method for the calibration of multi-channel frequency-domain data is described and results from the calibration are shown. The reproducibility and systematic errors are discussed. Image reconstructions from calibrated data measured of two inhomogeneous phantoms are given.

Publication IV

In this paper, difference data measured with the HUT frequency-domain optical tomography system is compared with the UCL MONSTIR time-domain system. Measured data from the two systems are compared with simulated data from a three-dimensional FEM solver. The FEM solver is validated with a Monte Carlo simulation program. Image reconstructions from the difference data measured using an inhomogeneous and a homogeneous phantom are given for a variety of measurement times, and the quality of measured data and the reconstructed images are evaluated as a function of imaging time using a variety of quantitative criteria.

Publication V

Optical topographic study of cortical hemodynamic changes on the right motor cortex induced by transcranial magnetic stimulation of the left motor cortex. This is a study of the cortical hemodynamic change which takes place in the right motor cortex when TMS is applied to the left motor cortex. The effect was found to be a decrease in amplitude at 830 nm during stimulation, while right-hand finger tapping was found to cause an increase in the same signal.

Publication VI

Bilateral near-infrared spectroscopic imaging of hemodynamic changes due to auditory stimulation in neonates. Ten neonates were subjected to optical imaging of the auditory areas on both hemispheres during an auditory stimulus paradigm.

Author's contribution

Publication I: My primary contribution was writing section 4 on instrumentation and experimental methods and section 5.3 on optical imaging of the brain. I wrote most of the introduction and discussion and contributed to the other sections in the form of editing and giving advice.

Publication II: I designed and implemented the electronics and mechanics of the single-channel instrument apart from the following: the IF amplifier of the PLL, the laser diode current supply, and the laser diode heat sink. I designed and implemented the control software except for parts of the temperature control algorithm. I tested the instrument as a whole, carried out the phantom measurements, the phase-amplitude cross-talk measurements, calibrated the data, calculated the simulated reference data, and wrote the manuscript.

Publication III: I designed the RF electronics of the multichannel system and the shielding mechanics apart from the laser diode mount. I implemented the electronics and mechanics together with the group and tested the RF electronics and the operation of the tomographic system as a whole. I designed and implemented the software lock-in amplifier, parts of the control software, the high voltage calibration method and integrated the three calibration stages together. I measured and analyzed the data used in the paper, calculated the reconstructions with Dr. Schweiger, and wrote the manuscript apart from the section on the reconstruction algorithm.

Publication IV: I measured the data with the HUT instrument, designed and implemented the Monte Carlo simulation program, calculated the simulated data using FEM and Monte Carlo, calculated the RMS differences between the model and measured difference data, calculated the reconstructions from the data measured with both systems, analysed the images, and wrote the manuscript apart from Sect. 2.1.1 on the UCL system, the part of Sect. 2.2 concerning FEM, and some editing.

Publication V: I performed the experiments together with the group, participated in the design of the experiments and the design of the analysis software, analyzed the in situ data, and wrote the manuscript.

Publication VI: I participated in the measurements, in the design of the analysis software and the experimental setup, and wrote the manuscript.

References

Additional references on diffuse optical imaging are included at the end of Publication I.

[1] *The Physics of Medical Imaging*, Ed. S. Webb, Institute of Physics Publishing (1992).

[2] Z.-P. Liang and P. C. Lauterbur, *Principles of Magnetic Resonance Imaging: A Signal Processing Perspective*, IEEE Press (2004).

[3] A. Schmermund, M. R Bell, L. O. Lerman, E. L. Ritman, J. A. Rumberger, Quantitative Evaluation of Regional Myocardial Perfusion Using Fast X-Ray Computed Tomography, Herz **22**: 29-39 (1997).

[4] S. Ogawa, T. M. Lee, A. R. Kay, and D. W. Tank, Brain magnetic resonance imaging with contrast dependent on blood oxygenation, Proc. Nat. Acad. Sci. USA **87**: 9868-72 (1990).

[5] N. D. Volkow, B. Rosen, L. Farde, Imaging the living human brain: Magnetic resonance imaging and posiron emission tomography, Proc. Nat. Acad. Sci. USA. **94**: 2787-8 (1997).

[6] F. F. Jöbsis, Noninvasive infrared monitoring of cerebral and myocardial oxygen sufficiency and circulatory parameters, Science **198**: 1264-7 (1977).

[7] D. Grosenick, H. Wabnitz, H. H. Rinneberg, K. T. Moesta, Development of a time-domain mammograph and first in vivo applications, Appl. Opt, **38**: 2927-2943 (1999).

[8] E. M. C. Hillman, J. C. Hebden, M. Schweiger, H. Dehghani, F. E. W Schmidt, D. T. Delpy, S. R. Arridge, Time resolved optical tomography of the human forearm, Phys. Med. Biol **46**: 1117-1130 (2001).

[9] M. A. Franceschini and D. A. Boas, Noninvasive measurement of neuronal activity with near-infrared optical imaging, Neuroimage **21**: 372-386 (2004).

[10] A. Li, E. L. Miller, M. E. Kilmer, T. J. Brukilacchio, T. Chaves, J. Stott, Q. Zhang, T. Wu, M. Chorlton, R. H. Moore, D. B. Kopans, and D. A. Boas, Tomographic optical breast imaging guided by three-dimensional mammography, Appl. Opt. **42**: 5181-5190 (2003).

[11] G. Strangman, D. A. Boas, and J. P. Sutton, Non-invasive neuroimaging using near-infrared light, Biol. Psychiatr. **52**: 679-693 (2002).

[12] J. C. Hebden, A. Gibson, R. Yusof, N. Everdell, E. M. C Hillman, D. T. Delpy, S. R. Arridge, T. Austin, J. H. Meek, and J. S. Wyatt, Three-dimensional optical tomography of the premature infant brain, Phys. Med. Biol. **47**: 4155-4166 (2002).

[13] J. C. Hebden, A. Gibson, T. Austin, R. Yusof, N. Everdell, D. T. Delpy, S. R. Arridge, J. H. Meek, and J. S. Wyatt, Imaging changes in blood volume and oxygenation in the newborn infant brain using three-dimensional optical tomography, Phys. Med. Biol. **49**: 1117-1130 (2004).

[14] J. C. Hebden, H. Veenstra, H. Dehghani, E. M. C. Hillman, M. Schweiger, S. R. Arridge, and D. T. Delpy, Three dimensional time-resolved optical tomography of a conical breast phantom, Appl. Opt. **40**: 3278-3287 (2001).

[15] B. Chance, E. Anday, S. Nioka, S. Zhou, L. Hong, K. Worden, C. Li, T. Murray, Y. Ovetsky, D. Pidikiti, and R. Thomas, A novel method for fast imaging of brain function, non-invasively, with light, Opt. Expr. **2**: 411-423 (1998).

[16] L. Szmedra, J. Im, S. Nioka, B. Chance, and K. W. Rundell, Hemoglobin/myoglobin oxygen desaturation during alpine skiing, Med. Sci. Sports Exerc. **33**: 232-236 (2001).

[17] H. Dehghani, B. W. Pogue, S. P. Poplack, and K. D. Paulsen, Multiwavelength three dimensional near infrared tomography of the breast: initial simulation, phantom and clinical results, Appl. Opt. **42**: 135-145 (2003).

[18] B. J. Tromberg, O. Coquoz, J. B. Fishkin, T. Pham, E. R. Anderson, J. Butler, M. Cahn, J. D. Gross, V. Venugopalan, D. Pham, Non-invasive measurements of breast tissue optical properties using frequency-domain photon migration, Phil. Trans. Royal Society London B **352**: 661-668 (1997).

[19] M. A. Franceschini, K. T. Moesta, S. Fantini, G. Gaida, E. Gratton, H. Jess, W. W. Mantulin, M. Seeber, P. M. Schlag, and M. Kaschke, Frequency-domain instrumentation enhances optical mammography: initial clinical results, Proc. Nat. Acad. Sci. USA **94**: 6468-6473 (1997).

[20] M. Kohl-Bareis, H. Obrig, J. Steinbrink, J. Malak, K. Uludag, and A. Villringer, Noninvasive monitoring of cerebral blood flow by a dye bolus method: Separation of brain from skin and skull signals, J. Biomed. Opt. **7**: 464-470 (2002).

[21] J. P. Culver, R. Choe, M. J. Holboke, L. Zubkov, T. Durduran, A. Slemp, V. Ntziachristos, B. Chance, and A. G. Yodh, Three-dimensional diffuse optical tomography in the parallel plane transmission geometry: Evaluation of a hybrid frequency domain/continuous wave clinical system for breast imaging, Med. Phys., **30**: 235-247 (2003).

[22] T. Durduran. Noninvasive measurements of tissue hemodynamics with hybrid diffuse optical methods. Med. Phys. **31**: 2178 (2004).

[23] D. J. Hawrysz, M. J. Eppstein, J. Lee, and E. M. Sevick-Muraca, Contrast enhanced three-dimensional optical tomography, Opt. Lett., **26**: 704-6 (2001).

[24] X. Intes, J. Ripoll, Y. Chen, S. Nioka, A. G. Yodh, and B. Chance, *In vivo* continuous-wave optical breast imaging enhanced with indocyanine green, Med. Phys. **30**: 1039-47 (2003).

[25] A. H. Hielscher, A. Y. Bluestone, G. S. Abdoulaev, A. D. Klose, J. Lasker, M. Stewart, U. Netz, and J. Beuthan, Near-infrared diffuse optical tomography, Dis. Markers **18**: 313-337 (2002).

[26] N. Iftimia, X. Gu, Y. Xu, and H. Jiang, A compact, parallel-detection diffuse optical mammography system, Rev. Sci. Instrum. **74**: 2836-42 (2003).

[27] E. Watanabe, Y. Yamashita, A. Maki, Y. Ito, H. Koizumi, Non-invasive functional mapping with multi-channel near infra-red spectroscopic topography in humans, Neurosci. Lett. **16**: 41-4 (1996).

[28] E. Hillman, Experimental and theoretical investigations of near infrared tomographic imaging methods and clinical applications, Ph. D. Thesis, University College London (2002).

[29] S. R. Arridge, Optical tomography in medical imaging, Inv. prob. **15**: R41-R93 (1999).

[30] M. Schweiger, and S. R. Arridge, Optical tomographic reconstruction in a complex head model using a priori region boundary information, Phys. Med. Biol. **44**: 2703-2722 (1999).

[31] A. H. Barnett, J. P. Culver, A. G. Sorensen, A. Dale, D. A. Boas, Robust inference of baseline optical properties of the human head with three-dimensional segmentation from magnetic resonance imaging, Appl. Opt. **42**: 3095-3108 (2003).

[32] V. Kolehmainen, S. R. Arridge, M. Vauhkonen, and J. P. Kaipio, Simultaneous reconstruction of internal tissue region boundaries and coefficients in optical diffusion tomography, Phys. Med. Biol. **45**: 3267-84 (2000).

[33] V. Kolehmainen, M. Vauhkonen, J. P. Kaipio, and S. R. Arridge, Recovery of piecewise constant coefficients in optical diffusion tomography, Opt. Expr. **7**: 468-480 (2000).

[34] C. H. Schmitz, H. L. Graber, H. Luo, I. Arif, J. Hira, Y. Pei, A. Bluestone, S. Zhong, R. Andronica, I. Soller, Ramirez N, Barbour SLS, and Barbour RL. Instrumentation and calibration protocol for imaging dynamic features in dense-scattering media by optical tomography, Appl. Opt. **39**, 6466-6486 (2002).

[35] C. H. Schmitz, M. Löcker, J. M. Lasker, A. H. Hielscher, and R. L. Barbour, Instrumentation for fast functional optical tomography, Rev. Sci. Instrum. **73**: 429-439 (2002).

[36] S. Nioka, Y. Yung, M. Schnall, S. Zhao, S. Orel, C. Xie, B. Chance, and S. Solin, Optical imaging of breast tumor by means of continuous waves, Adv. Exp. Med. Biol. **411**: 227-232 (1997).

[37] A. M. Siegel, J. J. A. Marota, and D. A. Boas, Design and evaluation of a continuous-wave diffuse optical tomography system, Opt. Expr. **4**: 287-298 (1999).

[38] C. Li, H. Zhao, and H. Jiang, A multi-spectral three-dimensional optical mammography system, OSA Biomedical Topical Meeting Technical Digest, Optical Society of America, Washington, DC, WF19 (2004).

[39] R. M. Danen, Y. Wang, X. D. Li, W. S. Thayer, and A. G. Yodh, Regional imager for low-resolution functional imaging of the brain with diffusing near-infrared light, Photochem. Photobiol. **67**: 33-40 (1998).

[40] J. P. Culver, R. Choe, M. J. Holboke, L. Zubkov, T. Durduran, A. Slemp, V. Ntziachristos, B. Chance, and A. G. Yodh, Three-dimensional diffuse optical tomography in the parallel plane transmission geometry: Evaluation of a hybrid frequency domain/continuous wave clinical system for breast imaging, Med. Phys., **30**: 235-247 (2003).

[41] T. O. McBride, B. W. Pogue, S. Jiang, U. L. Österberg, and K. D. Paulsen, A parallel-detection frequency-domain near-infrared tomography system for hemoglobin imaging of the breast in vivo, Rev. Sci. Instrum. **72**: 1817-1824 (2001).

[42] B. Chance, M. Cope, E. Gratton, N. Ramanujam, and B. Tromberg, Phase measurement of light absorption and scatter in human tissue, Rev. Sci. Instrum. **69**: 3457-3481 (1998).

[43] N. Ramanujam, C. Du, H. Y. Ma, and B. Chance, Sources of phase noise in homodyne and heterodyne phase modulation devices used for tissue oximetry studies, Rev. Sci. Instrum. **69**: 3042-54 (1998).

[44] I. Nissilä, K. Kotilahti, K. Fallström, and T. Katila, Instrumentation for the accurate measurement of phase and amplitude in optical tomography, Rev. Sci. Instrum. **73**: 3306-12 (2002).

[45] I. Nissilä, T. Noponen, K. Kotilahti, T. Tarvainen, M. Schweiger, L. Lipiäinen, S. Arridge, and T. Katila, Instrumentation and calibration methods for the multichannel measurement of phase and amplitude in optical tomography, submitted to Rev. Sci. Instrum.

[46] E. M. C. Hillman, J. C. Hebden, F. E. W. Schmidt, S. R. Arridge, M. Schweiger, H. Dehghani, and D. T. Delpy, Calibration techniques and datatype extraction for time-resolved optical tomography, Rev. Sci. Instrum. **71**: 3415-27 (2000).

[47] J. C. Hebden, F. M. Gonzalez, A. Gibson, E. M. C. Hillman, R. Yusof, N. Everdell, D. T. Delpy, G. Zaccanti, and F. Martelli, Assessment of an in situ temporal calibration method for time-resolved optical tomography, J. Biomed. Opt. **8**: 87-92 (2003).

[48] T. Tarvainen, V. Kolehmainen, M. Vauhkonen, A. Vanne, A. Gibson, S. R. Arridge, M. Schweiger, and J. P. Kaipio, Computational calibration method for optical tomography, accepted for publication in Appl. Opt. (2004).

[49] J. Riley, H. Dehghani, M. Schweiger, S. R. Arridge, J. Ripoll, and M. Nieto-Vesperinas, 3D optical tomography in the presence of void regions, Opt. Expr. **7**: 462-467 (2000).

[50] J. Heino, E. Somersalo, Estimation of optical absorption in anisotropic background, Inv. Prob. **18**: 559-573 (2002).

[51] R. J. Gaudette, D. H. Brooks, C. A. DiMarzio, M. E. Kilmer, E. L. Miller, T. Gaudette, and D. A. Boas, A comparison study of linear reconstruction techniques for diffuse optical tomographic imaging of absorption coefficient, Phys. Med. Biol. **45**: 1051-1070 (2000).

[52] D. A. Boas, M. A. O'Leary, B. Chance, and A. G. Yodh, Detection and characterization of optical inhomogeneities with diffuse photon density waves: a signal-to-noise analysis, Appl. Opt. **36**: 75-92 (1997).

[53] V. Ntziachristos, B. Chance, and A. G. Yodh, Differential diffuse optical tomography, Opt. Expr. **5**: 230-242 (1999).

[54] T. Durduran, J. P. Culver, M. J. Holboke, X. D. Li, and L. Zubkov, Algorithms for 3D localization and imaging using near-field diffraction tomography with diffuse light, Opt. Expr. **4**: 247-262 (1999).

[55] W. Zhu, Y. Wang, Y. Yao, J. Chang, H. L. Graber, and R. L Barbour, Iterative total least-squares image reconstruction algorithm for optical tomography by the conjugate gradient method, J. Opt. Soc. Am. A **14**: 799-807 (1997).

[56] Y. Yao, Y. Wang, Y. Pei, W. Zhu, R. L. Barbour, Frequency-domain optical imaging of absorption and scattering distributions by a Born iterative method, J. Opt. Soc. Am. A **14**: 325-342 (1997).

[57] R. Roy, and E. M. Sevick-Muraca, An active constrained truncated Newton method for optical tomography, J. Opt. Soc. Am. A **17**: 1627-41 (2000).

[58] M. J. Eppstein, D. E. Dougherty, T. L. Troy, and E. M. Sevick-Muraca, Biomedical optical tomography using dynamic parameterization and Bayesian conditioning on photon migration measurements, Appl. Opt. **38**: 2138-50 (1999).

[59] X. Li, D. N. Pattanayak, T. Durduran, J. P. Culver, B. Chance, and A. G. Yodh, Near-field diffraction tomography with diffuse photon density waves, Phys. Rev. E **61**: 4295-4309 (2000).

[60] H. Jiang, K. Paulsen, U. Österberg, B. Pogue, and M. Patterson, Simultaneous reconstruction of absorption and scattering images in turbid media from near-infrared frequency-domain data, Opt. Lett. **20**: 2128-30 (1995).

[61] M. A. O'Leary, D. A. Boas, B. Chance, and A. G. Yodh, Experimental images of heterogeneous turbid media by frequency-domain diffusing-photon tomography, Opt. Lett. **20**: 426-428 (1995).

[62] S. R. Arridge and W. R. B. Lionheart, Non-uniqueness in diffusion-based optical tomography, Opt. Lett. **23**: 882-884 (1998).

[63] S. R. Arridge, J. C. Hebden, M. Schweiger, F. E. W. Schmidt, M. E. Fry, E. M. C. Hillman, H. Dehghani, and D. T. Delpy, A method for 3D time-resolved optical tomography, International Journal for Imaging Systems and Technology **11**: 2-11 (2000).

[64] F. E. W. Schmidt, M. E. Fry, E. M. C. Hillman, J. C. Hebden, and D. T. Delpy, A 32-channel time-resolved instrument for medical optical tomography, Rev. Sci. Instrum. **71**: 256-265 (2000).

[65] I. Nissilä, J. C. Hebden, D. Jennions, J. Heino, M. Schweiger, K. Kotilahti, T. Noponen, A. Gibson, S. Järvenpää, L. Lipiäinen, and T. Katila, A comparison between

difference data measured with a time-domain and a frequency-domain system for optical tomography, submitted to Rev. Sci. Instrum.

[66] T. Tarvainen, M. Vauhkonen, V. Kolehmainen, and J. P. Kaipio, A hybrid radiative transfer - diffusion model for optical tomography, submitted to Appl. Opt. (2003).

[67] J.-M. Perkkiö, Radiative Transfer Problem on Riemannian Manifolds, Master's thesis, Helsinki University of Technology (2003).

[68] D. A. Boas, T. Gaudette, and S. R. Arridge, Simultaneous imaging and optode calibration with diffuse optical tomography, Opt. Expr. **8**: 263-270 (2001).

[69] M. Schweiger, I. Nissilä, and S. Arridge, in preparation.

[70] J. J. Stott, J. P. Culver, S. R. Arridge and D. A. Boas, Optode Positional Calibration in Diffuse Optical Tomography, Appl. Opt. **42**: 3154-3162 (2003).

[71] M.-A. Franceschini, V. Toronov, M. E. Filiaci, E. Gratton, and S. Fantini, On-Line Optical Imaging of the Human Brain with 160 ms Temporal Resolution, Opt. Expr. **6**: 49-57 (2000).

[72] H. Koizumi, T. Yamamoto, A. Maki, Y. Yamashita, H. Sato, H. Kawaguchi and N. Ichikawa, Optical topography: practical problems and new applications, Appl. Opt. **42**: 3054-3062 (2003).

[73] H. Obrig, H. Israel, M. Kohl-Bareis, K. Uludag, R. Wenzel, B. Muller, G. Arnold, and A. Villringer, Habituation of the visually evoked potential and its vascular response: implications for neurovascular coupling in the healthy adult, Neuroimage **17**: 1-18 (2002).

[74] G. Yu, T. Durduran, D. Furuya, J. H. Greenberg, and A. G. Yodh, Frequency-domain multiplexing system for *in vivo* diffuse light measurements of rapid cerebral hemodynamics, Appl. Opt. **42**: 2931-9 (2003).

[75] S. Prince, V. Kolehmainen, J. P. Kaipio, M. A. Franceschini, D. Boas, and S. R. Arridge, Time-series estimation of biological factors in optical diffusion tomography, Phys. Med. Biol. **48:** 1491-1504 (2003).

[76] D. P. Klemer, R. L. Barbour, C. H. Schmitz, H. L. Graber, Y. Pei, R. E. Hardin, M. S. Katz, N. A. Franco, and A. G. Smeraldi, Multi-side near-infrared tomographic imaging of the brain, OSA Biomedical Topical Meeting Technical Digest, Optical Society of America, Washington, DC, WF35 (2004).

[77] M. Cope, The application of near-infrared spectroscopy to non-invasive monitoring of cerebral oxygenation in the newborn infant, Ph.D. Thesis, University College London (1991).

[78] J. Heiskala, I. Nissilä, T. Neuvonen, S. Järvenpää, and E. Somersalo, Modeling anisotropic light propagation in a realistic model of the human head, accepted for publication in Appl. Opt. (2004).

[79] D. A. Boas, J. P. Culver, J. J. Stott, and A. K. Dunn, Three dimensional Monte Carlo code for photon migration through complex heterogeneous media including the adult human head, Opt. Expr. **10**: 159-170 (2002).

[80] J. D. Riley, S. R. Arridge, Y. Chrysanthou, H. Dehghani, E. M. C. Hillman, and M. Schweiger: The radiosity diffusion model in 3D, Proc. SPIE 4431 (2001).

[81] H. Jiang, Optical image reconstruction based on the third-order diffusion equations, Opt. Expr. **4**: 241-6 (1999).

[82] A. H. Hielscher, R. E. Alcouffe, R. L. Barbour, Comparison of finite-difference transport and diffusion calculations for photon migration in homogeneous and heterogeneous tissues, Phys. Med. Biol. **43**: 1285-1302 (1998).

[83] H. Sato, T. Takeuchi, and K. L. Sakai, Temporal cortex activation during speech recognition: an optical topography study, Cognition **73**: B55-66 (1999).

[84] A. Kleinschmidt, H. Obrig, M. Requardt, K. D. Merboldt, U. Dirnagl, A. Villringer, and J. Frahm, Simultaneous recording of cerebral blood oxygenation changes during human brain activation by magnetic resonance imaging and near-infrared spectroscopy, J. Cereb. Blood Flow. Metab. **16**: 817-26 (1996).

[85] W. N. Colier, V. Quaresima, B. Oeseburg, and M. Ferrari, Human motor-cortex oxygenation changes induced by cyclic coupled movements of hand and foot, Exp. Brain Res. **129**: 45u7-61 (1999).

[86] H. Obrig, C. Hirth, J. G. Junge-Hulsing, C. Doge, T. Wolf, U. Dirnagl, and A. Villringer, Cerebral oxygenation changes in response to motor stimulation, J. Appl. Physiol. **81**: 1174-83 (1996).

[87] H. R. Heekeren, H. Obrig, R. Wenzel, K. Eberle, J. Ruben, K. Villringer, R. Kurth, and A. Villringer, Cerebral haemoglobin oxygenation during sustained visual stimulation – a near-infrared spectroscopy study, Philos. Trans. R. Soc. Lond. B Biol. Sci. **352**: 743-750 (1997).

[88] Y. Hoshi and M. Tamura, Detection of dynamic changes in cerebral oxygenation coupled to neuronal function during mental work in man, Neurosci. Lett. **150**: 5-8 (1993).

[89] A. Villringer, J. Planck, C. Hock, L. Schleinkofer, and U. Dirnagl, Near infrared spectroscopy (NIRS): a new tool to study hemodynamic changes during activation of brain function in human adults, Neurosci. Lett. **154**: 101-4 (1993).

[90] M. A. Franceschini, S. Fantini, J. J. Thompson, J. P. Culver, and D. A. Boas, Hemodynamic evoked response of the sensorimotor cortex measured non-invasively with near-infrared optical imaging, Psychophysiology **40**: 548-60 (2003).

[91] G. Strangman, J. Culver, J. Thompson, and D. Boas, A quantitative comparison of simultaneous BOLD fMRI and NIRS recordings during functional brain activation, Neuroimage **17**: 719 (2002).

[92] G. Gratton, M. R. Goodman-Wood, and M. Fabiani, Comparison of neuronal and hemodynamic measures of the brain response to visual stimulation: an optical imaging study, Hum. Brain Mapp. **13**: 13-25 (2001).

[93] A. K. Dunn, A. Devor, H. Bolay, M. L. Andermann, M. A. Moskowitz, A. M. Dale„ and D. A. Boas, Simultaneous imaging of total cerebral hemoglobin concentration, oxygenation, and blood flow during functional activation, Opt. Lett. **28**: 28-30 (2003).

[94] C. Hirth, H. Obrig, K. Villringer, A. Thiel, J. Bernarding, W. Muhlnickel, H. Flor, U. Dirnagl, and A. Villringer, Non-invasive functional mapping of the human motor cortex using near-infrared spectroscopy, NeuroReport **7**: 1977-81 (1996).

[95] R. Wenzel, H. Obrig, J. Ruben, K. Villringer, A. Thiel, J. Bernarding, U. Dirnagl, and A. Villringer, Cerebral blood oxygenation changes induced by visual stimulation in humans, J. Biomed. Opt. **1**: 399-404 (1996).

[96] T. Durduran, G. Yu, M. G. Burnett, J. A. Detre, J. H. Greenberg, J. Wang, C. Zhou, and A. G. Yodh, Diffuse optical measurement of blood flow, blood oxygenation, and metabolism in a human brain during sensorimotor cortex activation, Opt. Lett. **29**: 1766-8 (2004).

[97] D. P. Klemer, R. L. Barbour, C. H. Schmitz, H. L. Graber, Y. Pei, R. E. Hardin, M. S. Katz, N. A. Franco, A. G. Smeraldi, Multi-site near-infrared tomographic imaging of the brain, OSA Biomedical Topical Meeting Technical Digest, Optical Society of America, Washington, DC, WF35 (2004).

[98] T. Durduran, G. Yu, M. G. Burnett, C. Zhou, J. A. Detre, J. H. Greenberg, and A. G. Yodh, Diffuse optical measurements of oxygen metabolism in human brain during sensorimotor stimulus, OSA Biomedical Topical Meeting Technical Digest, Optical Society of America, Washington, DC, WE4 (2004).

[99] R. P. Kennan, S. G. Horovitz, A. Maki, Y. Yamashita, H. Koizumi, J. C. Gore, Simultaneous recording of event-related auditory oddball response using transcranial near infrared optical topography and surface EEG, Neuroimage **16**: 587-92 (2002).

[100] V. Toronov, A. Webb, J. H. Choi, M. Wolf, L. Safonova, U. Wolf, and E. Gratton, Study of local cerebral hemodynamics by frequency-domain near-infrared spectroscopy and correlation with simultaneously acquired functional magnetic resonance imaging, Opt. Expr. **9**: 417-427 (2001).

[101] V. Toronov, A. Webb, J. H. Choi, M. Wolf, A. Michalos, E. Gratton, and D. Hueber, Investigation of human cerebral hemodynamics by simultaneous near-infrared spectroscopy and functional magnetic resonance imaging, Med. Phys. **28**: 521-7 (2001).

[102] D. J. Mehagnoul-Schipper, B. Oeseburg, W. H. Hoefnagels, and R. W. Jansen, Simultaneous measurements of cerebral oxygenation changes during brain activation by near-infrared spectroscopy and functional magnetic resonance imaging in healthy young and elderly subjects, Hum. Brain. Mapp. **16**: 14-23 (2002).

[103] A. Oliviero, V. Di Lazzaro, O. Piazza, P. Profice, M. A. Pennisi, F. Della Corte, and P. Tonali, Cerebral blood flow and metabolic changes produced by repetitive magnetic brain stimulation, J. Neurol. **246**: 1164-8 (1999).

[104] Y. Noguchi, E. Watanabe, and K. L. Sakai, An event-related optical topography study of cortical activation induced by single-pulse transcranial magnetic stimulation, Neuroimage **19**: 156-162 (2003).

[105] K. Sakatani, S. Chen, W. Lichty, H. Zuo, and Y. P. Wang, Cerebral blood oxygenation changes induced by auditory stimulation in newborn infants measured by near-infrared spectroscopy, Early Hum. Dev. **55**: 229-36 (1999).

[106] M. Peña, A. Maki, D. Kovacic, G. Dehaene-Lamberts, H. Koizumi, F. Bouquet, and J. Mehler, Sounds and silence: An optical topography study of language recognition at birth, Proc. Nat. Acad. Sci. **100**: 11702-5 (2003).

[107] P. Zaramella, F. Freato, A. Amigoni, S. Salvadori, P. Marangoni, A. Suppjei, B. Schiavo, and L. Chiandetti, Brain auditory activation measured by near-infrared spectroscopy (NIRS) in neonates, Pediatr. Res. **49**: 213-9 (2001).

[108] S. Chen, K. Sakatani, W. Lichty, P. Ning, S. Zhao, and H. Zuo, Auditory-evoked cerebral oxygenation changes in hypoxic-ischemic encephalopathy of newborn infants monitored by near-infrared spectroscopy, Early Hum. Dev. **67**: 113-121 (2002).

[109] S. R. Hintz, D. A. Benaron, A. M. Siegel, A. Zourabian, D. K. Stevenson, and D. A. Boas, Bedside functional imaging of the premature infant brain during passive motor activation, J. Perinat. Med. **29**: 335-43 (2001).

[110] G. Taga, K. Asakawa, K. Hirasawa, and Y. Konishi, Hemodynamic responses to visual stimulation in occipital and frontal cortex of newborn infants: a near-infrared optical topography study, Early Hum. Dev. **75**: S203-210 (2003).

[111] T. Kusaka, K. Kawada, K. Okubo, K. Nagano, M. Namba, H. Okada, T. Imai, K. Isobe, and S. Itoh, Noninvasive optical imaging in the visual cortex in young infants, Hum. Brain Mapp. **22**: 122-132 (2004).

[112] M. Bartocci, J. Winberg, G. Papendieck, T. Mustica, G. Serra, and H. Lagercrantz, Cerebral hemodynamic response to unpleasant odors in the preterm newborn measured by near-infrared spectroscopy, Pediatr. Res. **50**: 324-330 (2001).

[113] Hamamatsu Photonics, Metal package photomultiplier tubes (R7400 series) and photosensor modules, Technical information (1998).

[114] Hamamatsu Photonics, H6780 photosensor module data sheet.

[115] Hamamatsu Photonics, H7442 photosensor module data sheet.

[116] Hamamatsu Photonics, Silicon avalanche photodiodes, Technical data sheet S-502 (1990).

[117] Hamamatsu Photonics, Photodiode and operational amplifier integrated with feedback resistance and capacitance, Technical data sheet (1994).

[118] D. A. Boas, M. A. O'Leary, B. Chance, and A. G. Yodh, Scattering of diffuse photon density waves from spherical inhomogeneous within turbid media: Analytic solution and applications, Proc. Nat. Acad. Sci. USA **91**: 4887-91 (1994).

[119] D. A. Boas, M. A. O'Leary, B. Chance, and A. G. Yodh, Detection and characterization of optical inhomogeneities with diffuse photon density waves: a signal-to-noise analysis, Appl. Opt. **36**: 75-92 (1997).

[120] D. A. Boas, M. A. O'Leary, B. Chance, and A. G. Yodh, Scattering and wavelength transduction of diffuse photon density waves, Phys. Rev. E **47**: R2999-R3002 (1993).

[121] M. A. O'Leary, D. A. Boas, B. Chance, and A. G. Yodh, Refraction of diffuse photon density waves, Phys. Rev. Lett. **69**: 2658-61 (1992).

[122] V. Toronov, E. D'Amico, D. Hueber, E. Gratton, B. Barbieri, and A. Webb, Optimization of the signal-to-noise ratio of frequency-domain instrumentation for near-infrared spectro-imaging of the human brain, Opt. Expr. **11**: 2717-29 (2003).

[123] H. Eda, I. Oda, Y. Ito, Y. Wada, Y. Oikawa, Y. Tsunazawa, M. Takada, Y. Tsuchiya, Y. Yamashita, and M. Oda, A. Sassaroli, Y. Yamada, and M. Tamura, Multichannel time-resolved optical tomographic imaging system, Rev. Sci. Instrum. **70**: 3595-3602 (1999).

[124] K. Alford and Y. Wickramasinghe, Phase-amplitude crosstalk in intensity modulated near infrared spectroscopy, Rev. Sci. Instrum. **71**: 2191-5 (2000).

[125] M. Firbank and D. T. Delpy, A design for a stable and reproducible phantom for use in near-infrared imaging and spectroscopy, Phys. Med. Biol. **38**: 847-853 (1993).

[126] *Handbook of transcranial magnetic stimulation*, Eds. A. Pascual-Leone, N. J. Davey, J. Rothwell, E. M. Wasserman, and B. K. Puri, Arnold Publishers (2002).

[127] R. J. Ilmoniemi, J. Virtanen, J. Ruohonen, J. Karhu, H. J. Aronen, R. Näätänen, and T. Katila, Neuronal responses to magnetic stimulation reveal cortical reactivity and connectivity, NeuroReport **8**: 3537-3540 (1997).

[128] S. Komssi, H. J. Aronen, J. Huttunen, M. Kesäniemi, L. Soinne, V. V. Nikouline, M. Ollikainen, R. O. Roine, J. Karhu, S. Savolainen, and R. J. Ilmoniemi, Ipsi- and contralateral EEG reactions to transcranial magnetic stimulation, Clin. Neurophys. **113**: 175-184 (2002).

[129] K. Kotilahti, I. Nissilä, M. Huotilainen, R. Mäkelä, N. Gavrielides, T. Noponen, P. Björkman, V. Fellman, and T. Katila, Bilateral hemodynamic responses to auditory stimulation in newborn infants, manuscript in preparation.